2019-04-01

Mesoscale Modeling of Shape Memory Alloys by Kinetic Monte Carlo–Finite Element Analysis Methods

Adam David Herron
Brigham Young University

Mesoscale Modeling of Shape Memory Alloys by Kinetic Monte Carlo-Finite Element Analysis Methods

Adam David Herron

A thesis submitted to the faculty of
Brigham Young University
in partial fulfillment of the requirements for the degree of

Master of Science

Eric R. Homer, Chair
David T. Fullwood
Oliver K. Johnson

Department of Mechanical Engineering

Brigham Young University

ABSTRACT

Mesoscale Modeling of Shape Memory Alloys by Kinetic
Monte Carlo-Finite Element Analysis Methods

Adam David Herron
Department of Mechanical Engineering, BYU
Master of Science

A coupled kinetic Monte Carlo – Finite Element Analysis (kMC–FEA) method is developed with a numerical implementation in the Scalable Implementation of Finite Elements at NASA (ScIFEN). This method is presented as a mesoscale model for Shape Memory Alloy (SMA) material systems. The model is based on Transition State Theory and predicts the nonlinear mechanical behavior of the 1st order solid–solid phase transformation between Austenite and Martensite in SMAs. The kMC–FEA modeling method presented in this work builds upon the work of Chen and Schuh [1, 2]. It represents a "bottom-up" approach to materials modeling and could serve as a bridge for future studies that attempt to link *ab initio* methods with phenomenological findings in SMA systems. This thesis presents the derivation of the kMC–FEA model, which is then used to probe the various responses expected in SMAs and verify the influence of model parameters on simulation behavior.

In a departure from the work of Chen and Schuh, the thermodynamic derivation includes an elastic transformation energy term, which is found to be a significant fraction of the total transformation energy and play an important role in the evolution of a simulation. Theoretical predictions of the model behavior can be made from this derivation, including expected transformation stresses and temperatures. A convergence study is presented as verification that the new elastic energy term proposed in this model is a reasonable approximation. A parameter sensitivity study is also presented, showing good agreement between theoretical predictions and the results of a full-factorial numerical exploration of model outputs.

Model simulation demonstrates the emergence of the shape memory effect, an important SMA behavior not shown by Chen and Schuh, along with the expected superelastic effect and thermal hysteresis. Further exploration of simulated model outputs presented in this work involves comparison with experimental data and predicted output values obtained from a separate phenomenological constitutive model. This comparison shows that the kMC–FEA method is capable of reproducing qualitative, but not yet quantitative, responses of real SMA material systems.

Discussion of each model parameter and its effects on the behavior of the model are presented as guidelines for future studies of SMA materials. A complete implementation of the method is contained in a new finite element software package (ScIFEN) that is available for future studies.

Keywords: kinetic Monte Carlo, Finite Element Analysis, Shape Memory Alloys, Superelastic, Hysteresis, Materials Modeling, ScIFEN

ACKNOWLEDGMENTS

Foremost, I would like to acknowledge my God for his bounteous creation and its limitless intricacy. I never cease to be amazed by the astonishing complexity and beautiful simplicity which emerges out of the universe He created.

This work was made possible by Brigham Young University and its sponsoring organization, The Church of Jesus Christ of Latter-day Saints, through the charitable donations of its members.

Next, I would like to acknowledge my advisor Eric Homer. He spent many hours guiding my energy and patiently persuading me to narrow the scope of this research. He helped me recognize and develop my talents to make this work possible.

This work would not have been possible without the help of Jacob Hochhalter, Vesselin Yamakov, Geoffrey Bomarito, and James Warner at the NASA Langley Research Center. They helped build the tools and provided the opportunity for me to join this great endeavor. My experience with them was funded by the National Aeronautics and Space Administration under a series of NASA Interns, Fellows, and Scholars (NIFS) internship opportunities.

I'd like to also acknowledge David and Deborah Herron for giving me a safe place to learn and ask questions from a young age. The apple doesn't fall far from the tree.

Finally, I'd like to acknowledge Janette Herron for her patience and support as I completed this work.

TABLE OF CONTENTS

LIST OF TABLES

LIST OF FIGURES

NOMENCLATURE

E_{fr}	Frictional Energy
E_I	Elastic inclusion energy
E_t	Transition activation energy
E_y	Young's Modulus
ε^{tr}	transformation strain
$G^{\ddagger}$	Transition state Gibbs Energy
G_1, G_2	Initial and final Gibbs Energies
γ_0	Transformation shear strain
ΔG	Difference between the final and initial Gibbs Energies
ΔG^{ch}	Difference between the final and initial chemical potential
ΔG^{el}	Difference between the final and initial elastic potential
ΔG^{sf}	Difference between the final and initial surface energy
ΔG^{i}	Difference between the final and initial interfacial energies
ΔS_0	Difference between final and initial entropy at thermal equilibrium
σ^I	Inclusion stress
σ^A	Applied stress
Δt_{int}	Internal (kMC) time step
Δt_{ext}	External (FEA) time step
ν	Poisson's Ratio
ν_0	Attempt frequency
ξ	Random number
ω	Transformation rate of a single transformation zone
ω_{tot}	Sum of transformation rates

CHAPTER 1. INTRODUCTION

Shape Memory Alloys (SMAs) are a useful branch of engineering materials that exhibit large nonlinearities in their thermo-mechanical response. These nonlinearities, which include superelasticity and the shape memory effect, are what give SMAs their name and the desirable properties that make them useful, but also make modeling these materials challenging.

If SMAs are to be useful for engineers and designers, their thermo-mechanical response must be predictable in the range of conditions of their intended use. A host of phenomenological material models have been developed to describe the response of SMAs under a limited set of conditions. These models work well if the material is used under these conditions, but do not allow investigators to explore material behavior outside the model's fitted region. Other models, based on first-principles and atomistic calculations, accurately describe the behavior of SMAs, but are only computationally feasible at short length and time scales.

This study extends the work of Chen and Schuh [1, 2] and focuses on bridging the gap between the atomistic scale phenomena which govern SMA behavior and continuum scale modeling techniques. In order to bridge this gap, a finite element solver is coupled with kinetic Monte Carlo (kMC) methods to stochastically evolve the microstructural state of the model according to phase transition probabilities

1.1 SMA Background Information

Shape Memory alloys get their name from the shape memory effect, a property which allows them to recover a large amount of inelastic deformation upon heating [3]. SMAs also exhibit a property known as pseudoelasticity (or superelasticity) at elevated temperatures. This allows them to undergo a significant amount of pseudo-elastic deformation upon loading, which is completely recovered upon unloading (see Figure 1.1).

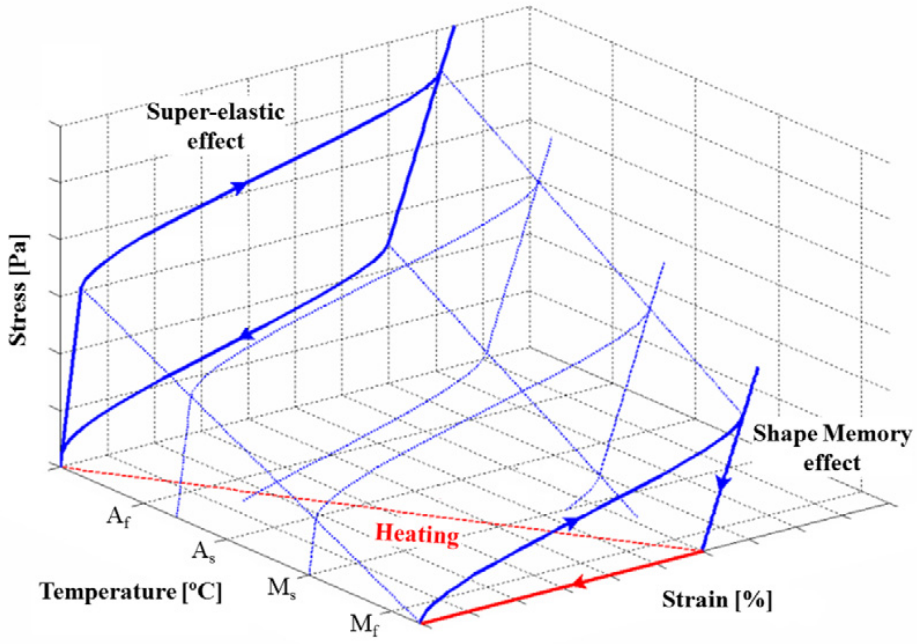

Figure 1.1: Used with permission from [4], this figure is an excellent illustration of the stress-strain response of SMAs over a range of temperatures. The super-elastic effect is observed at higher temperatures while the shape memory effect is observed at lower temperatures

Figure 1.1 shows how the nature of the stress–strain curve of a Shape Memory Alloy changes when the temperature is changed. At high temperatures, the Austenite phase is favored and phase transformation to Martensite is accomplish via stress induced phase transformation. At lower temperatures, the Martensite phase becomes stable at zero stress. Thus, stress induced transformation strain is not automatically recovered at low stress, but may be recovered completely through the application of heat and thermally induced transformation from Martensite to Austenite.

Although the shape memory effect was first discovered in Cd-Au alloys in the early 1930's, investigation in earnest did not begin until 1963, when Ni-Ti alloys were discovered to exhibit the shape memory effect near room temperature [4]. Since that time, SMAs have been a hot topic in materials science and engineering.

The unique non-linear thermo-mechanical response of SMAs is primarily due to their reversible martensitic transformation. That is, they undergo a reversible, first order, solid state phase transformation, from a highly-ordered Austenite phase to a more-disordered Martensite phase, when subjected to a temperature shift or stress field [5]. For more detailed descriptions of this

transformation and why it is necessary for the shape memory effect and pseudoelasticity in SMAs, see [6, 7].

1.2 Applications

SMAs are rapidly finding applications in a variety of fields, including:

- **Aerospace:** SMAs typically have a density which lies between aluminum and steel [4]. The shape memory effect also gives some SMAs a high actuation energy density, making them attractive candidates for lightweight aerospace actuation mechanisms like that used in the variable area jet nozzle design [8–10].
- **Vibrational Damping Structures:** SMAs have the ability to dissipate a large amount of mechanical energy through their pseudoelastic hysteresis [11, 12].
- **Medical and Dental Devices:** Ni-Ti, in particular, is highly biocompatible and can exhibit its superelastic response at the temperature of the human body. This makes it useful for applications such as orthodontics [13] and heart stents [14].
- **Damage-Sensing Composites:** Research performed at NASA Langley has investigated the feasibility of using embedded SMA particles as sensors to detect fatigue crack growth in structural composites [15–23]. Stress fields located near crack tips induce transformation of sensory particles, which emit detectable acoustic signals – see figure 1.2.

1.3 Modeling

As stated previously, the Martensitic transformation is what governs the behavior of SMAs. At the atomistic level, the physics governing the martensitic transformation for many SMA systems can be accurately modeled using molecular dynamics simulation (MD) and *ab initio* methods [5, 24–28]. SMA transformation behavior is very sensitive to the chemical composition of the alloy and exploration of new chemical compositions can readily be made using MD [24]. Such methods are impractical for everyday engineering and design applications, however, because they access

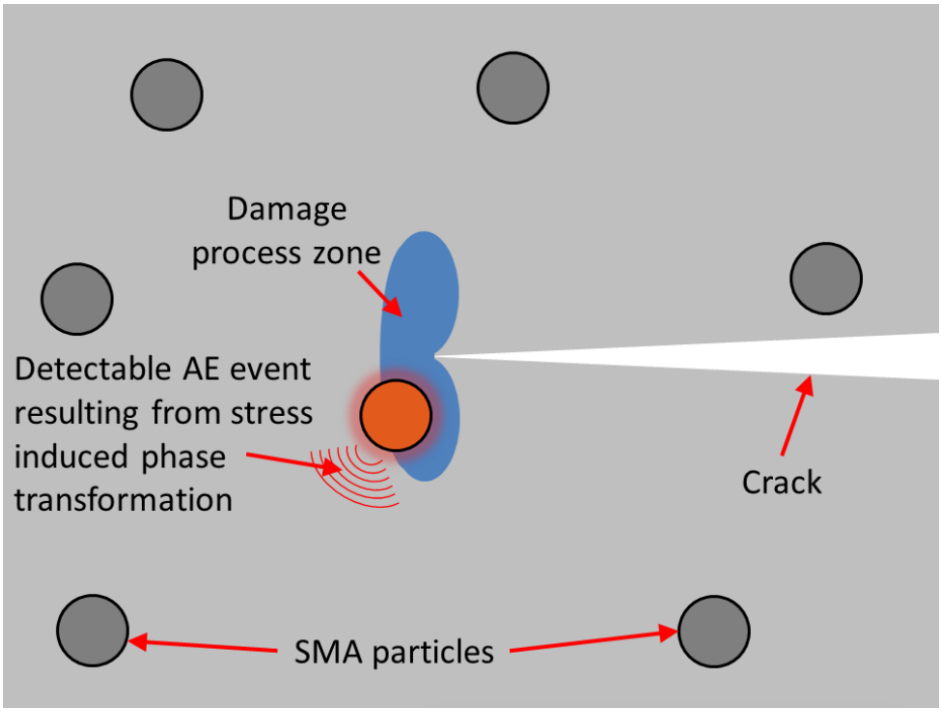

Figure 1.2: Used with permission from [17], this figure illustrates the use of SMA materials as embedded sensors for use in smart composite structures

only very short time and length scales. Such methods are very useful for determining material properties and behaviors which can be course-grained to predict bulk material behavior.

In contrast, traditional finite element analysis (FEA) methods are much more practical for component-scale analysis. They operate at the continuum level, allow for rapid prototyping, iterative design, and optimization; but require continuum scale material models. The large nonlinearities, anisotropic character, and strong dependence on temperature, load history, and composition make SMAs difficult to characterize using traditional continuum scale FEA material models which do not account for these factors. In response to this daunting challenge, a host of new and interesting material models have been proposed and implemented, which capture certain aspects of SMA behavior very well. An extensive review of many of these models is given by Cisse [3].

Of particular interest is a model developed by Lagoudas *et al* [7, 12, 29–35]; a thermodynamic continuum model, fit to experimental data. It shows good agreement with experimental data under a wide range of temperature and loading conditions for particular chemical compositions. This model is a subject of comparison/contrast in this work.

Recently, Chen and Schuh proposed a new SMA model, based on kinetic Monte Carlo (kMC) methods and implemented in the Abaqus FEA solver [1, 2]. This model allows groups of elements to transform stochastically according to transition state theory. Some major advantages of this model are that it predicts SMA phenomena, rather than fitting for them; it tracks the local evolution and propagation of transformation fronts; and it operates on a physical time scale. This model framework seemed promising, since it potentially accesses longer length and time scales than accessible using MD simulations, but also claimed not to require phenomenological fitting. It was hoped that an extension of this model would allow for the optimization of SMA chemical composition for use in sensory particle applications and it was to this end that we selected the kMC–FEA model framework for adaptation.

In the present work, we extend the methods of Chen and Schuh mainly through a re-derivation of the relevant thermodynamics, a re-implementation of their model in the Scalable Implementation of Finite Elements at NASA (ScIFEN) FEA code, model exploration, demonstration of the emergent shape memory effect, a parameter sensitivity analysis, and comparison with experimental data and fitted phenomenological predictions made using the Lagoudas model. Since kMC–FEA methods are still very new to SMA modeling, this work is mainly an exploration of the coupled kMC–FEA modeling framework as a useful tool for studying SMA material systems. It highlights some of the advantages and limitations of the framework. It may also shed new light on SMA systems and may serve as a useful starting point for future SMA modeling efforts

CHAPTER 2. METHODS

In this chapter, the kinetic Monte Carlo–Finite Element Analysis (kMC–FEA) method is developed. A summary of the relevant thermodynamics and kinetics is given and an implementation of the kMC algorithm is presented. Theoretical predictions of model behavior are made based on thermodynamic and kinetic reasoning. Methods for a parametric study are given to show how comparison is made between theoretically predicted outputs and simulated results. Methods are also outlined for comparison of model results with experimental data and with predictions made by a commonly used phenomenological constitutive model.

2.1 kMC–FEA Model Development

The kinetic Monte Carlo – Finite Element Analysis model consists of a finite element solver coupled with a kMC algorithm. The kMC algorithm controls the evolution of the model by imposing an eigenstrain on stochastically selected elements to mimic phase transformation in that region. In short, the kMC algorithm takes the stress and phase state of the model as input and calculates local rates of transformation within the mesh based on material energetics and thermodynamic principles. The output for the kMC algorithm is then the duration of the elapsed time for that event to occur, as well as a list of which integration points to transform and the phase/variant to which they will transform. A corresponding eigenstrain, dependent upon the current and future phase/variant, is then applied to the transforming points.

This type of model is based on transition state theory and assumes that small regions (transformation zones) in an elastic solid have inelastic transformation kinetics based on an Arrhenius law. Such a model was proposed by Argon and Bulatov [36], explored and developed for amorphous metal systems by Homer and Schuh [37] and further applied to phase transformation of Shape Memory Alloy systems by Chen and Schuh [1, 2], of which this work is a further extension.

2.1.1 Energetics

The Austenite-Martensite phase transformation which underlies the pseudoelastic Effect and shape memory effect in SMA material systems can be modeled as a transformation of discrete regions of volume Ω_0. The rate at which these regions activate (or transform between phases) is predicted by transition state theory according to the following rate equation:

$$\omega = \nu_0 \exp -\frac{E_t \Omega_0}{kT} \tag{2.1}$$

where ν_0 is the attempt frequency (assumed to be on the order of the Debye frequency), k is the Boltzmann constant, and T is the absolute temperature. E_t is the transformation energy barrier (Note: all energy and entropy values considered here are per-unit-volume values).

Additional modeling may be warranted to characterize the barrier for specific material systems, but for the purposes of this generic SMA model, we assume that the activated (or transition) state has Gibbs energy equal to the average of the pre- and post-transformation Gibbs energies plus a constant:

$$G^{\ddagger} = \frac{1}{2}(G_1 + G_2) + E_{fr} \tag{2.2}$$

The constant E_{fr} is theoretically positive for both forward and reverse transformation and represents the additional kinetic energy required to overcome the energy barrier at the transition state. It could also include the additional potential energy of the transition configuration, any frictional energy or energy dissipated via plasticity in the material. Further discussion of this parameter is given in section 4.1.2.

The transformation rate kinetics are governed by the transformation energy barrier E_t, which is simply the difference between the current Gibbs energy (G_1) and the Gibbs energy of the transition state ($G^{\ddagger}$). An illustration of this concept is shown in Figure 2.1, which represents the Gibbs energy as a function of the extent of transformation. The activation energy is the difference in Gibbs energy between the current configuration and the transition state.

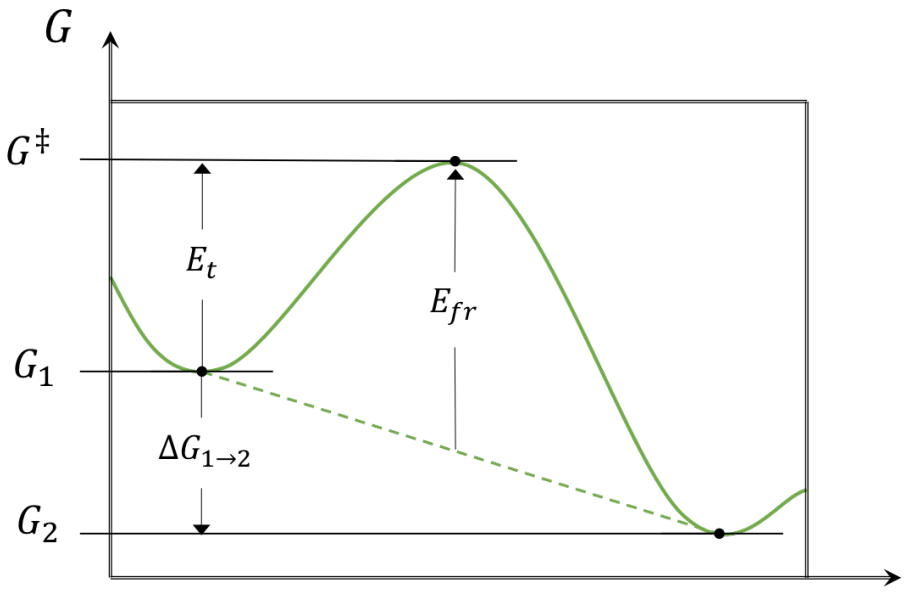

Figure 2.1: The Gibbs free energy as a function of the extent of transformation from an initial to final transformation states. Gibbs energies are given in energy-per-unit volume.

$$\begin{aligned} E_t &= G^{\ddagger} - G_1 \\ &= \frac{1}{2}(G_1 + G_2) + E_{fr} - G_1 \\ &= \frac{1}{2}\Delta G_{1\to 2} + E_{fr} \end{aligned} \tag{2.3}$$

Like Chen and Schuh, we consider the difference in Gibbs Energy between two phases to be a combination of the differences in their chemical potential, elastic energy, free surface energy and interface energies:

$$\Delta G = \Delta G^{ch} + \Delta G^{el} + \Delta G^{sf} + \Delta G^{i} \tag{2.4}$$

Like Chen and Schuh, we linearize the chemical potential (see Figure 2.2) by assuming that the heat capacity is constant and consistent between phases near the equilibrium temperature (T_0), such that the transformation enthalpy $\Delta H \approx \Delta H_0$ and entropy $\Delta S \approx \Delta S_0$ are also constant, the change in chemical potential reduces to:

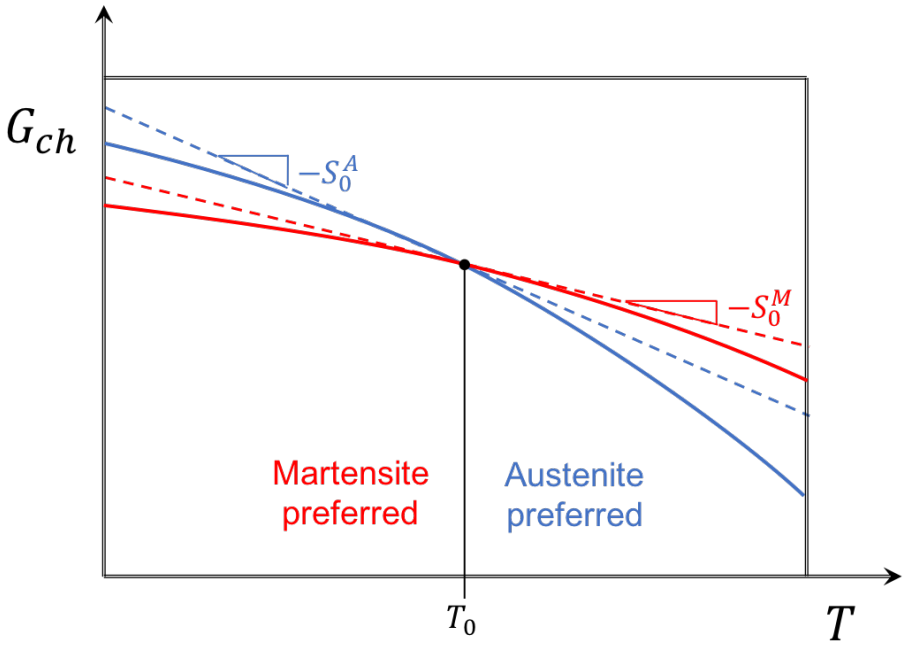

Figure 2.2: The chemical potential, linearized at the equilibrium temperature, as a function of temperature. The slope of the chemical potential is the entropy, which we assume is constant for this study

$$\Delta G^{ch} = -\Delta S_0 (T - T_0) \tag{2.5}$$

Unlike Chen and Schuh, we estimate the comlete elastic energy of transformation. The elastic energy of a transforming inclusion ΔG^{el} is formulated by Eshelby [38]. For an elliptical or ellipsoidal elastic inclusion undergoing a uniform transformation strain ε^{tr} in the presence of an applied stress field σ^A, the elastic energy has a closed form solution:

$$\Delta G^{el} = -\frac{1}{2}\sigma^I \varepsilon^{tr} - \sigma^A \varepsilon^{tr} \tag{2.6}$$

The inclusion stress σ^I is uniformly distributed throughout an ellipsoidal inclusion and can be readily calculated via the material stiffness, transformation strain, and the appropriate Eshelby tensor. For transformation strains of equivalent magnitude but differing strain directions, transforming in an isotropic material, the quantity $-\frac{1}{2}\sigma^I \varepsilon^{tr}$ is a positive constant, which we will denote E_I. This lets us rewrite equation 2.6 as:

$$\Delta G^{el} = E_I - \sigma^A \varepsilon^{tr} \tag{2.7}$$

Also in departure from the method of Chen and Schuh, the surface and interface energies have been neglected in this study. Combining equations 2.4, 2.5, and 2.7 yields:

$$E_t = -\frac{1}{2}\Delta S_0 (T - T_0) - \frac{1}{2}\sigma^A \varepsilon^{tr} + \frac{1}{2}E_I + E_{fr} \tag{2.8}$$

Care should be taken when applying equation 2.8 that the correct values are used for ΔS_0, and ε^{tr}, as they are dependent upon the initial and final phase or variant.

2.1.2 Kinetic Monte Carlo Algorithm

A modified rejection-free kMC algorithm is employed to stochastically select transformation events and update the simulation time step. The algorithm proceeds according to the following steps:

1. Local stresses are solved using finite element methods.

2. A transformation energy E_t is calculated for each of the MxN possible transformation events according to equation 2.8. Each event represents one of the N transformation zones in the model transforming to one of the M other allowed phases/variants. Each transformation energy is then used to calculate a corresponding transformation rate according to equation 2.1. Transformation rates are capped at the attempt frequency ν_0.

3. The total transformation rate is computed as the sum of these transformation rates: $\omega_{tot} = \sum_{i=1}^{NxM} \omega_i$ and a random number $\xi_1 \sim u(0,1]$ is generated and to determine the internal (kMC) time step:

$$\Delta t_{int} = -\frac{ln(\xi_1)}{\omega_{tot}} \tag{2.9}$$

4. If $\Delta t_{int} \leq \Delta t_{ext}$, the internal (kMC) timestep is used and the algorithm proceeds to step 5. Else if $\Delta t_{int} > \Delta t_{ext}$, the external (FEA) timestep is used, no transformation occurs on this iteration, and the algorithm proceeds to step 7.

$$\Delta t = min\{\Delta t_{int}, \Delta t_{ext}\} \tag{2.10}$$

5. A second random number $\xi_2 \sim u(0,1]$ is generated and used to select the transformation event to activate, with each event's probability of being selected being proportional to its transformation rate ω_i.

6. The selected transformation is imposed by updating the phase/variant and eigenstrain state of the selected transformation zone's integration points.

7. The simulation time is incremented by the time step selected in step 4, the loading conditions $\sigma(t)$, $\varepsilon(t)$, or $T(t)$ are updated, and the steps are repeated from step 1 until termination conditions are met.

2.1.3 Finite Element Coupling

Step 1 of the rejection-free kMC algorithm involves solving for local stresses via finite element methods. This is important since the local stress environment is a strong function of both the global (time dependent) loading conditions and neighboring transformation strains (see Figure 2.4). Some important considerations need to be made when implementing the finite element model.

The Eshelby inclusion energy calculation, used in determining the transformation energy of each transformation zone, assumes the transforming region to be an elliptical (or ellipsoidal for the 3-dimensional case) inclusion, surrounded by an infinite matrix. Energies calculated for shapes varying much from elliptical and non-infinite mediums can introduce substantial error [39]. To this end, and due to the discrete, non-elliptical nature of typical finite elements, mesh refinement techniques were employed to approximate elliptical transformation zones. No attempt is made in this study to correct for the non-infinite nature of the surrounding medium or the potential non-uniform stiffness of surrounding medium.

The inclusion transformation energy (E_I) can be computed using γ_0 and the Eshelby tensor. For this study, we use a 2-Dimensional finite element model with in-plane transformation strains. E_I for this geometry can be approximated as:

$$E_I = \frac{E_y \gamma_0^2}{4(1-\nu^2)} \tag{2.11}$$

where E_y is the average elastic modulus between the Austenite and Martensite phases. Some error is introduced during this approximation, since the Austenite and Martensite phases do not have the same stiffness and the inclusions do not transform in an infinite matrix. Further discussion on this point is presented in Chapter 4.4.

A convergence study is performed, similar to that performed by Homer and Schuh [37], comparing the elastic strain energy observed in a finite element mesh undergoing an inclusion transformation in its interior and the energy predicted for an ideal ellipsoidal inclusion of equal volume using the Eshelby equations. For this study, a small spherical inclusion, composed of a variable number of 10-node tetrahedral elements, is subjected to a predefined martensitic transformation eigenstrain in ScIFEN. Comparison is made between the elastic energy change reported by the finite element solver and theoretical predictions for an inclusion given by the Eshelby equations multiplied by the inclusion volume. Since the Eshelby inclusion energy is reported as a per-unit-volume quantity, scaling it by the inclusion volume normalizes these values for direct comparison. The number of elements is then varied through mesh refinement techniques and the comparison is repeated.

As expected, the difference in predicted elastic strain energy between the two methods drops dramatically as the mesh refinement increases and more elements are used to approximate the ellipsoid. It is concluded that approximately 27 quadratic tetrahedral elements were sufficient to bring the energy calculation within approximately 5 percent error (see Figure 2.3), which was deemed suitable for this study. Using a larger number of elements could bring the relative error in transformation energy down an additional order of magnitude, but would come at high computational cost.

2.2 Implementation details

To highlight the capability of the kMC–FEA model framework in producing superelastic hysteresis, temperature hysteresis, and the shape memory effect, model parameters are chosen in well-behaved regions of the parameter space which produce clean output stress–strain and

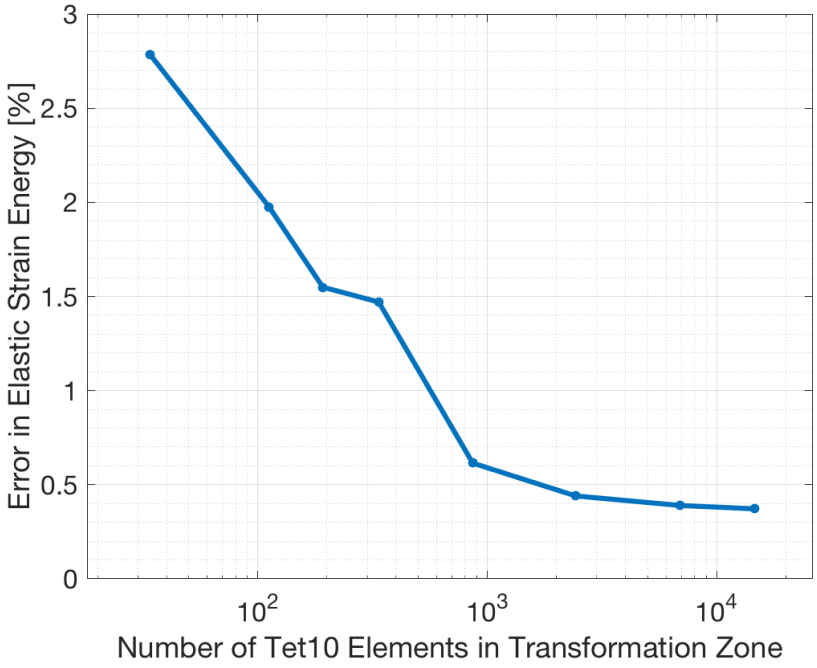

Figure 2.3: Results of the convergence study, showing the absolute relative error between the theoretical elastic strain energy for a transforming inclusion, predicted by Eshelby, and the numerically simulated elastic strain energy of an inclusion, modeled in ScIFEN.

Table 2.1: Nominal parameters used for kMC-FEA model simulations illustrating the superelastic stress hysteresis (see Figure 3.1) and temperature hysteresis (see Figure 3.2).

Variable	Value	Units
ΔS_0	-0.1155	MPa/K
γ_0	0.0165	-
E_y	27500	MPa
ν	0.3	-
E_I	2.1243	MPa
E_{fr}	0.1217	MPa
Ω_0	1e-25	m^3
T_M	212	K
T_A	253	K
T	303	K
Δt_{ext}	0.001	ps
ν_0	1.0831e2	THz

temperature–strain curves. Parameters used for the superelastic stress hysteresis and temperature hysteresis simulations are given in Table 2.1.

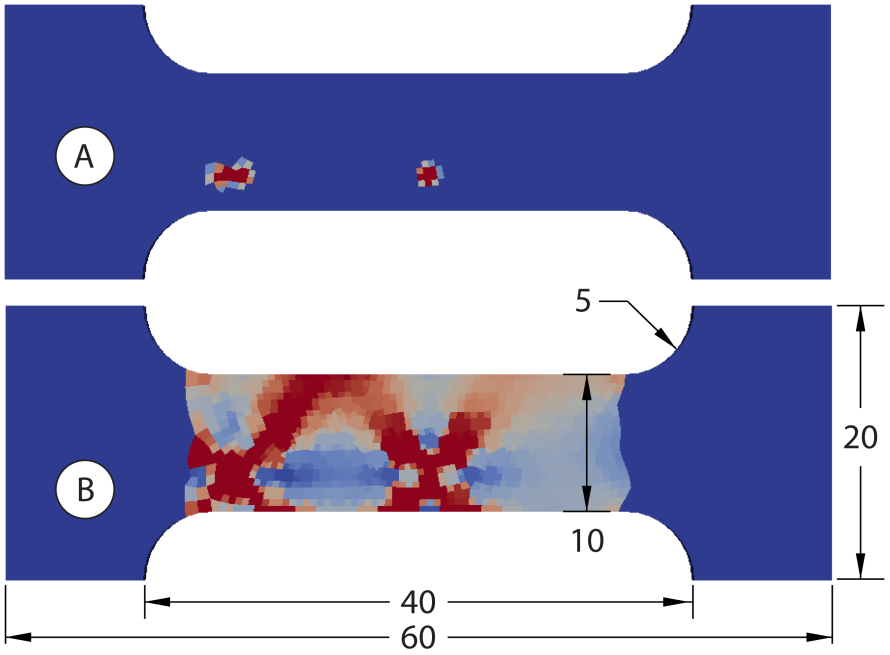

Figure 2.4: Illustration showing (A) the transforming phase (Blue = Austenite & Red = Martensite) and (B) the transformation rate. Note that the rate of transformation zones is affected by the transformation of its neighbors (Red elements have high transformation rates)

The finite element mesh, used frequently throughout this study, is shown visually in Figure 2.4. It contains a total of 1593 8-node hexahedral (Hex8) elements throughout the model. Only the gauge section, which is shaded clearly in Figure2.4(B) is allowed to transform from Austenite to Martensite. This gauge section has 1367 Hex8 elements, each divided into 8 integration points, for a total of 10936 separate transformable integration points. These transformable integration points are course-meshed into circular transformation zones of radius 2.5, for a total of 82 independent transformation zones. Figure 2.4(A) shows three individual transformation zones which have transformed to the Martensite phase (Red).

SMA material systems typically have a variety of crystallographic orientations of Martensite (or Martensite variants) to which the highly symmetric Austenite phase can transform [6]. For simplicity and to maintain material generality, we only consider one variant of Martensite in this work.

To ensure that transformation zones are approximately elliptical/ellipsoidal, a separate mesh of transformation zones, composed of the individual integration points within the finite element mesh is constructed. For 2-dimensional model, a hexagonal mesh is used. For 3-dimensional

models, a mesh of truncated octahedra is used. This ensures that transformation zones are approximately elliptical/ellipsoidal and that the mesh volume is completely tessellated.

The kMC algorithm is implemented directly into the source code for the "Scalable Implementation of Finite Elements at NASA" (ScIFEN), a new massively parallel finite element analysis software package being developed by a group at the NASA Langley Research Center [40]. Collaboration with this group has given us access to the source code, which is under export control. Having access to the FEA source code is a great advantage for this type of model implementation, since eigenstrains need to be imposed within transformation zones, a behavior which is challenging to implement in other FEA solvers. An example input script for the kMC–FEA ScIFEN implementation is included in Appendix B

2.2.1 Theoretical Transformation Points

In order to predict the behavior of the kMC–FEA model and to compare that behavior to experimental data and other SMA models, it is desirable to have predictions for the critical stresses and temperatures that induce phase transformation. This model has the potential initiate transformation under a number of circumstances. When the whole model is in the Austenite phase, it can begin transforming to Martensite due to an increase in stress (at $\tau = \tau_{MS}$) or a decrease in Temperature (at $T = T_{MS}$). Likewise, the model begins transforming from Martensite to Austenite with decreasing stress (at $\tau = \tau_{AS}$ or increasing temperature (at $T = T_{AS}$). The difference between these stresses represents the stress hysteresis ($\Delta\tau_H$) at constant temperature or the temperature hysteresis (ΔT_H) at constant stress.

Thermodynamic principles would suggest that the material will begin transformation when the Gibbs energy of transformation is zero:

$$\Delta G = -\frac{1}{2}\Delta S_0(T - T_0) - \frac{1}{2}\sigma^A \varepsilon^{tr} + \frac{1}{2}E_I + E_{fr} = 0 \tag{2.12}$$

Substituting the appropriate transformation stress ($\sigma^A = \tau_{MS}$, τ_{AS}, or τ), temperature ($T = T_{MS}$, T_{AS}, or T), entropy ($-\Delta S_0$ or ΔS_0) and direction of transformation strain ($\varepsilon^{tr} = \gamma_0$ or $-\gamma_0$) depending upon whether the model is transforming to Martensite or Austenite, then solving for the various critical stresses and temperatures yields:

$$\tau_{MS} = \frac{1}{\gamma_0}\left\{-\Delta S_0(T - T_0) + E_I + 2E_{fr}\right\} \tag{2.13}$$

$$\tau_{AS} = \frac{1}{\gamma_0}\left\{-\Delta S_0(T - T_0) - E_I - 2E_{fr}\right\} \tag{2.14}$$

$$T_{MS} = T_0 - \frac{1}{\Delta S_0}\left\{\tau\gamma_0 - E_I - 2E_{fr}\right\} \tag{2.15}$$

$$T_{AS} = T_0 + \frac{1}{\Delta S_0}\left\{-\tau\gamma_0 - E_I - 2E_{fr}\right\} \tag{2.16}$$

Making the theoretical stress and temperature hysteresis values:

$$\begin{aligned} \Delta\tau_H &= \tau_{MS} - \tau_{AS} \\ \Delta\tau_H &= \frac{2}{\gamma_0}\left\{E_I + 2E_{fr}\right\} \end{aligned} \tag{2.17}$$

$$\begin{aligned} \Delta T_H &= T_{AS} - T_{MS} \\ \Delta T_H &= -\frac{2}{\Delta S_0}\left\{E_I + 2E_{fr}\right\} \end{aligned} \tag{2.18}$$

2.3 Experimental and Computational Comparison

Comparison is made with the output of this new kMC–FEA model, experimental data, and the output of a calibrated model, developed by Lagoudas et al. [29, 32, 33]. Experimental data was obtained by [33] standard uniaxial dogbone tensile testing according to ASTM standard [41]. Parameters for the Lagoudas model were fit to this experimental superelastic stress hysteresis data, and are shown in Table 1 of [33]. These parameters were also used to estimate appropriate parameters for the kMC–FEA model, which are listed in Table 2.2.

Despite their similarity, some effort is required to translate the model parameters used in the Lagoudas model to suitable parameters for use in the kMC–FEA model as the variable parameters

Table 2.2: kMC-FEA Model Parameters for Model Comparison Simulation

Variable	Value	Units
ΔS_0	-0.3727	MPa/K
γ_0	0.0515	
E_y	26.4e3	MPa
ν	0.33	
E_I	26.2710	MPa
E_{fr}	-26.00	MPa
Ω_0	1e-24	m^3
T_M	236.70	K
T_A	267.35	K
T	298.15	K
Δt_{ext}	0.005	ps
ν_0	1.0831e2	THz

differ. For instance, the temperature parameters T_A and T_M required for the kMC–FEA model could be translated as the average of $[T_{AS},T_{AF}]$ and $[T_{MS},T_{MF}]$ respectively. Some parameters are the same, as in $H_{min} = \gamma_0$.

The parameters C^M and C^A in the Lagoudas model represent the derivative of the forward and reverse transformation stresses with respect to temperature. Hence:

$$C^M(T - T_M) - C^A(T - TA) = \Delta\tau_H = \frac{2}{\gamma_0}(E_I + 2E_{fr})$$

$$E_{fr} = \frac{\gamma_0}{4}\left(C^M(T - T_M) - C^A(T - T_A)\right) - \frac{1}{2}E_I \tag{2.19}$$

$$\tau_0 = \frac{1}{2}(\tau_{MS} + \tau_{AS}) = \frac{1}{2}\left(C^A(T - T_A) + C^M(T - T_M)\right)$$

substitution from Equations 2.13 & 2.14 allows for estimating ΔS_0:

$$\Delta S_0 = \frac{-\gamma_0}{2(T - T_0)}\left(C^A(T - T_A) + C^M(T - T_M)\right) \tag{2.20}$$

A qualitative comparison is made between experimental data, the output of the kMC–FEA simulation, and the output of a fitted phenomenological model. The simulation is that of a supere-

lastic stress–strain hysteresis curve, similar to the superelastic simulation shown in Figure 3.1, but with experimentally estimated values for the input parameters. Most notably, a much higher strain value is used in this simulation (5.15% vs. 1.65%). The results of this comparative study are given in section 3.3 and further discussion is given in section 4.2.

CHAPTER 3. RESULTS

The general behavior of the kMC–FEA model is described in the context of three non-deterministic, emergent behaviors: 1). superelastic stress hysteresis, 2). temperature hysteresis, and 3). the shape memory effect. A parameter study is presented, showing the tendency of the model output to change predictably with perturbation to the input parameters. Finally, a comparison is made between the output of the kMC–FEA model, experimentally obtained data, and a commonly used phenomenological model, fitted to the experimental data.

3.1 kMC-FEA Model Behavior

3.1.1 Superelastic Stress Hysteresis

Figure 3.1 illustrates the results of a dog-bone tensile simulation using the kMC-FEA model with the parameters indicated in Table 2.1. The figure includes both the stress–strain curve and snapshots of the simulation cell at various points indicated on the curve. The simulation consists of a tensile sample undergoing a single loading cycle at a temperature above the Austenite Finish temperature.

As illustrated in Figure 3.1, the simulation begins at point (1), unstrained and unstressed, in the Austenite phase. The top grip section of the sample is held fixed and a displacement boundary condition, applied at the bottom grip section, imposes a constant strain rate on the sample, deforming it elastically between points (1) and (2). At point (2), the sample appears to reach a critical stress level (σ_{MS}) at which point Martensite nucleates and begins to grow in the Austenite sample, halting the increase in stress through transformation strain accommodation.

The Martensite usually nucleates and grows in a band structure, angled diagonally from the tensile axis. Point (3) is the point at which approximately 50% of the sample has transformed to Martensite. When the simulation reaches point (4) at a slightly higher apparent stress level (σ_{MF}),

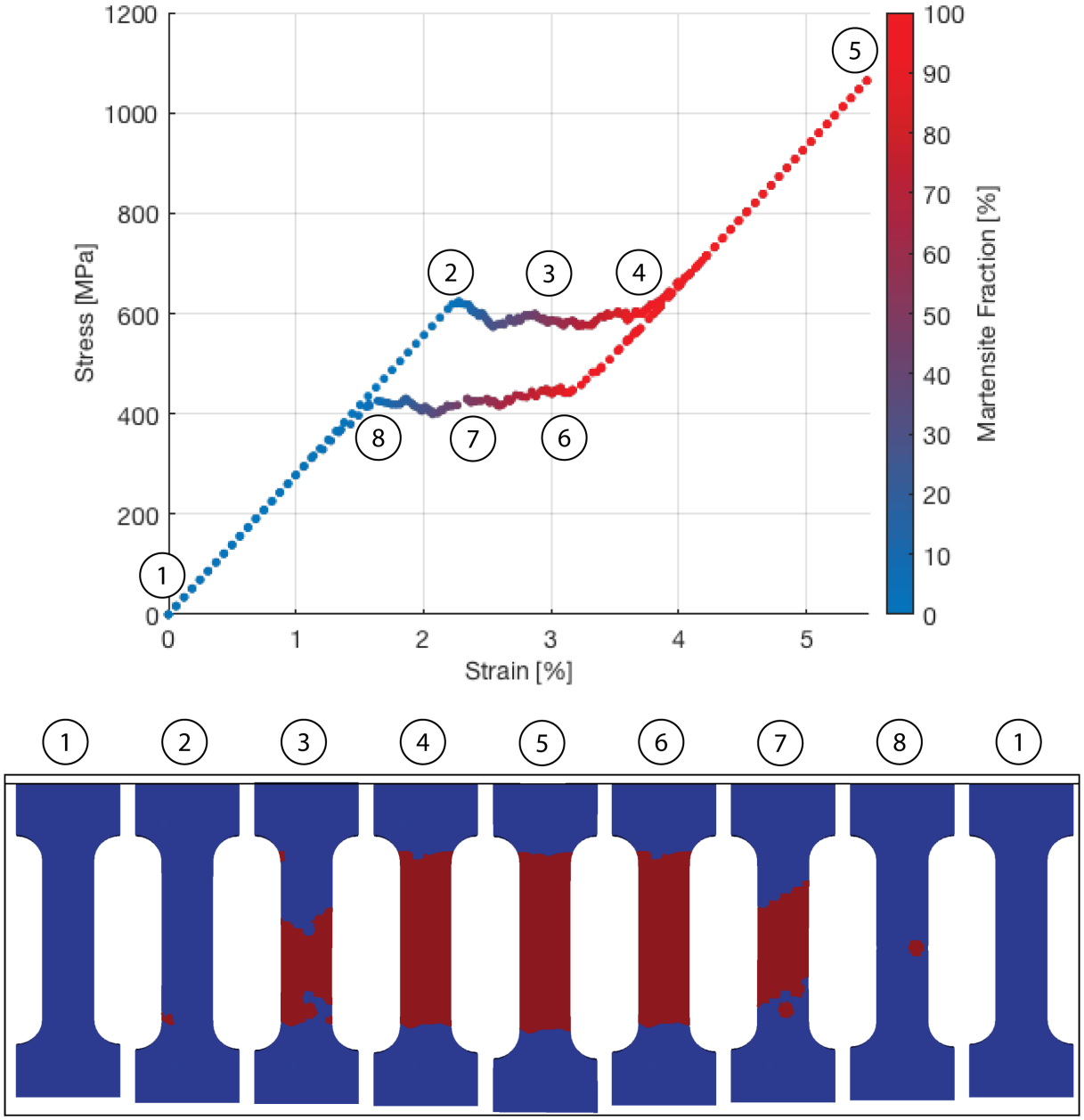

Figure 3.1: Top: Stress–Strain plot, showing the bulk behavior of the kMC-FEA model when pulled in tension at superelastic temperatures. Note the clear hysteresis between forward stress during loading and reverse stress during unloading. Bottom: Snapshots of the transformation process from the kMC-FEA model simulation, showing the propagation of phase fronts. Red elements represent Martensite phase while blue elements represent Austenite phase

the sample has completely transformed to Martensite and further loading between points (4) and (5) is elastic deformation of the Martensite phase.

Once loading reaches its maximum stress and strain at point (5), the loading rate is reversed and unloading begins. Strain is recovered elastically between points (5) and (6). The critical stress (σ_{AS}) at point (6) is the stress at which Austenite begins to grow back out of the Martensite. During reverse transformation Austenite grows out of the Martensite in the opposite direction through the sample, consuming the transformed Martensite elements from the outside of the sample inward.

Little change in the stress magnitude occurs as the simulation passes through the 50% Austenite mark at point (7), until the apparent critical stress (σ_{AF}) at point (8) is reached. At this point, the model has completely returned to the Austenite phase and strain recovery is elastic again between points (8) and (1).

The simulation represented in Figure 3.1 is representative of the general features of this kind of dogbone tensile cycle simulation, which uses the kMC-FEA material model. It should be noted that the output stress magnitudes (σ_{MS}, σ_{MF}, σ_{AS}, and σ_{AF}) and the shape of the stress–strain curve are not model parameters, but rather are emergent from the simulation, measured from the output of the model. Although the model is non-deterministic, the theoretical calculations presented in Equations 2.13–2.18 actually are a fair predictor of the model behavior in this region of the parameter space. Deviations from theoretically predicted behavior are attributed to effects not accounted for in the thermodynamics, such as meshing, stress concentration points, etc. Further discussion of this presented in sections 3.2 and 4.4

3.1.2 Temperature Hysteresis

Figure 3.2 illustrates the results of a thermal loading simulation. In this case, the free end of the dogbone is unconstrained in the tensile direction and allowed to expand freely as the model transforms from Austenite to Martensite and then back to Austenite due to temperature cycling.

At point (1), the simulation begins in the Austenite phase at a temperature above the Austenite Finish temperature (T_{AF}). The sample is then ”quenched” by dropping the simulation temperature at a constant rate over time. When the model reaches point (2), the temperature has reached an apparent critical temperature (T_{MS}), at which point the transformation rate is high enough that transformation to Martensite begins. The sample continues to transform until point

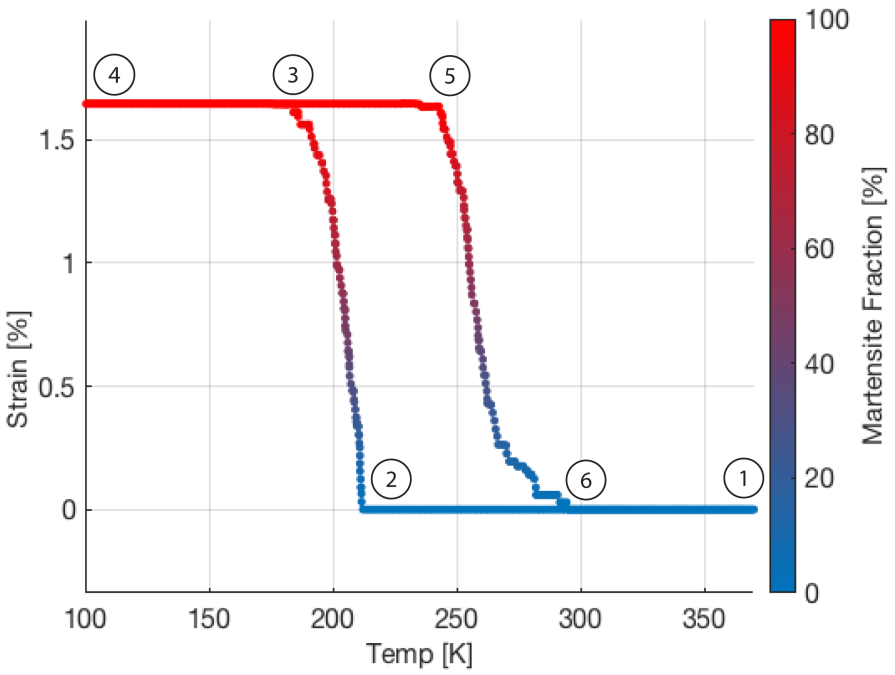

Figure 3.2: Temperature–Strain plot, showing the output of a thermal cycling simulation using the kMC-FEA material model with one unconstrained boundary condition. Note the clear temperature hysteresis which occurs between forward and reverse thermal transformation

(3), when it has completely transformed to Martensite. The observed temperature we measure at point (3) is termed the Martensite Finish temperature (T_{MF}).

The simulation continues to cool until it reaches the minimum temperature at point (4) and then the thermal loading rate reverses. The sample temperature rises to point (5), when it begins transforming from Martensite back to Austenite and we measure the observed Austenite Start temperature (T_{AS}). The sample has completely transformed to Austenite at point (6) and the Austenite Finish temperature (T_{AF}) is recorded. Then the temperature is raised to its original value and the cycle is completed.

Similar to the critical stresses measured from the output of the stress hysteresis cycle simulation, the four critical temperatures measured during thermal cycling (T_{MS}, T_{MF}, T_{AS}, and T_{AF}) are emergent from the stochastic simulation rather than given as input parameters. They are strongly related to the model input parameters T_A and T_M, but are also affected by simulation conditions, such as loading rate and the presence of candidate nucleation sites in the finite element model.

It should be noted that no Martensite twinning or self-accommodating microstructure patterns develop in this temperature cycling process due to the fact that, in the model simulations presented in this work, only a single Martensite variant is allowed to transform from the Austenite. The model is capable of allowing any number of Martensite variants, but for simplicity's sake, only a single variant is included in this study. It is expected that self-accommodation would occur if multiple variants were included.

3.1.3 Shape Memory Effect

When a tensile simulation, like that used to show stress hysteresis in Figure 3.1, is performed at a temperature below the Austenite Finish temperature (T_{AF}), the shape memory effect is observed. The shape memory effect is a property exhibited by SMAs wherein permanent transformation strain is retained after unloading, but then recovered by subsequent heating of the material above the Austenite Finish temperature, as illustrated in Figure 1.1.

A simulation of the shape memory effect is presented in Figure 3.3. A tensile simulation is performed, starting with no strain at point (1). A monotonically increasing stress load is applied at the free end of the model between points (1) and (4). Transformation from Austenite to Martensite begins at point (2) and full transformation to Martensite occurs at point (3). At point (4) loading reverses, monotonically decreasing from the peak loading stress and back to zero applied stress at point (5).

At point (5), the tensile loading cycle has completed. The model has relaxed elastically and is now in an unstressed state. Note that a significant amount of retained transformation strain remains at point (5), as the material is still completely in the Martensite phase.

Between point (5) and point (1) the fixed end is left unconstrained and simulation temperature is raised steadily from its initial value to a value above the Austenite Finish temperature (T_{AF}). As the temperature is raised, the Martensite is transformed gradually to Austenite and the transformation strain is completely recovered by point (1).

Demonstration of the shape memory effect is an important extension of the work of Chen and Schuh [1, 2] and validation of the kMC–FEA method in general. The fact that the shape memory effect emerges from the model by simply lowering the simulation temperature is good evidence that the model is capturing at least part of the physical nature of the material transformation system.

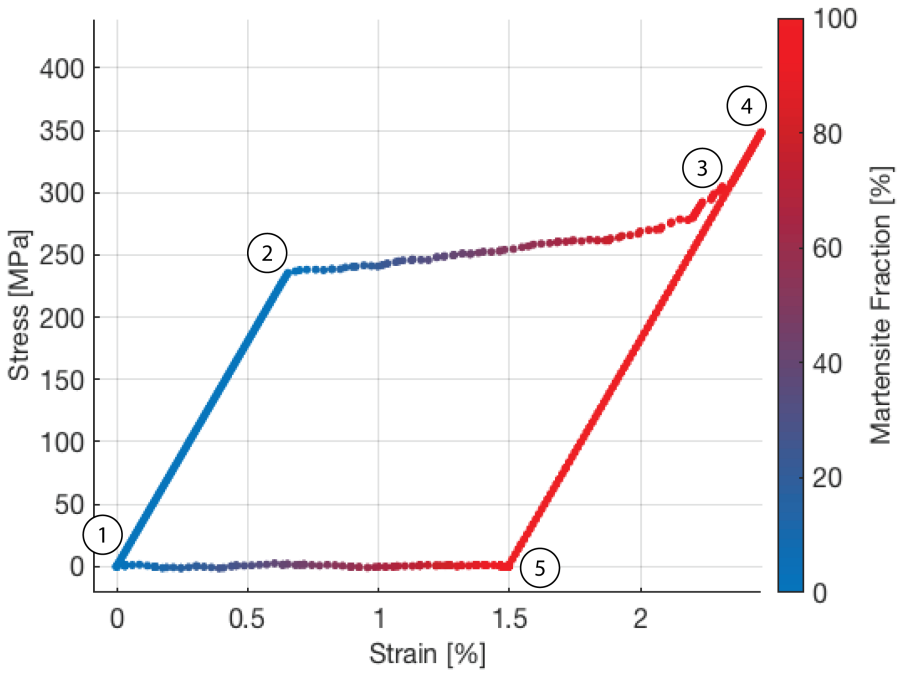

Figure 3.3: Stress–Strain plot illustrating the shape memory effect. The stress–strain curve is the result of a tensile simulation performed below the Austenite Finish temperature. Strains produced by transformation are relieved by increasing the temperature above the Austenite Finish temperature at point (5), inducing reverse transformation and causing the material to ”remember” its original shape and fully recover the transformation strain.

3.2 kMC-FEA Parameter Study

Whereas we seek to understand the predictive value of the kMC–FEA model and whereas the predictions made by the theoretical predictions derived in Chapter 2 differ from those observed in the model output, a parameter study is performed to characterize the general relationships between input, expected output, and measured output of the model in a small, well-behaved region of the parameter space.

The nominal point chosen from the parameter space is shown in Table 3.1. Using this nominal point as a baseline center point, superelastic tensile simulations, like the one shown in Figure 3.1 are run, varying 4 independent parameters at 3 different levels with a full factorial design of experiment, for a total of $3^4 = 81$ full tensile simulation cycles. Level values for the parameter study are given in Table 3.2

Table 3.1: Nominal parameter values used in the parameter study

Variable	Value	Units
ΔS_0	-0.1875	MPa/K
γ_0	0.015	-
E_y	36e3	MPa
ν	0.33	-
E_{fr}	0.7388	MPa
Ω_0	1e-25	m^3
T_M	240.0	K
T_A	280.0	K
T	300.0	K
Δt_{ext}	0.001	ps
ν_0	1.0831e2	THz

Table 3.2: Parameter study input parameter level values

Input	Units	Low	Mid	High
T	K	290	300	310
ΔS_0	MPa/K	-0.1775	-0.1875	-0.1975
E_{fr}	$MPa]$	0.6388	0.7388	0.8388
γ_0	-	0.0140	0.0150	0.0160

From the simulations, the model stresses and strains are recorded, along with 5 model output values: (τ_{MS}, τ_{MF}, τ_{AS}, τ_{AF}, $\Delta\tau_H$). These are the same critical stress values identified at points (2), (4), (6), & (8) in Figure 3.1 These output values are successfully fit to a 4 dimensional hyperplane of the input space with an R^2 value of 0.9641 to effectively calculate a gradient across the input/output space at this point. To compare these results to those predicted in Section 2.2.1 a theoretically predicted gradient can also be calculated by differentiating Equations 2.13 – 2.17 with respect to the four varied input values of T, ΔS_0 , E_{fr}, and γ_0. These differentials are defined in Appendix A.

Predictions made using equations A.1 – A.12 are compared side-by side with tensile simulation outputs from the parameter study in Table 3.3. This table shows that with few exceptions, the output measured from parameter study simulation runs is quite consistent with theoretically predicted values. Most notably, the partial derivatives of the forward and reverse transformation stresses are very consistent with theoretically predicted values in both magnitude and direction.

Table 3.3: Parameter Study Results – Theoretical predictions and simulation measurement values for the outputs of the superelastic hysteresis parameter study with relative error reported. The top row contains the nominal values for the output variables and the bottom four rows contain comparison of the gradient values with respect to each of the 4 design parameters.

	τ_{MS}			τ_{AS}			$\Delta\tau_H$		
	Theoretical	Measured	Error	Theoretical	Measured	Error	Theoretical	Measured	Error
Value	750.00	730.71	3%	250.00	389.40	56%	500.01	341.31	32%
$\frac{\partial}{\partial T}$	12.50	12.51	0%	12.50	13.25	6%	0.00	-0.73	-
$\frac{\partial}{\partial \Delta S_0}$	-2666.67	-2597.00	3%	-2666.67	-2807.00	5%	0.00	210.00	-
$\frac{\partial}{\partial E_{fr}}$	133.33	137.08	3%	-133.33	-130.34	2%	266.67	267.42	0%
$\frac{\partial}{\partial \gamma_0}$	-29800.57	-31538.00	6%	-36866.10	-31249.00	15%	7065.53	-289.00	104%

Although the stochastic nature of the kMC–FEA model makes *a priori* model behavior predictions challenging, this parameter study shows that local regions of the parameter space may have a fairly predictable output space. This suggests that, with some effort, model outputs could be optimized to fit experimental data. Further discussion of the parameter sensitivity is discussed in section 4.1.2.

3.3 Model Comparison

The results of the comparison between the kMC–FEA model, the Lagoudas model, and experimental stress-strain data, as described in section 2.3, are illustrated in Figure 3.4.

The experiment and both models start unstressed and load elastically before beginning transformation to the Martensite phase. The experiment begins transformation at a little over 400 MPa and slightly decreases its stress after nucleation before transforming at nearly constant stress until full transformation is complete. The Lagoudas model fits this forward transformation process nearly exactly, with the exception of missing the slight decrease in stress, right after the nucleation point. The uncalibrated kMC–FEA model seems to overshoot the forward transformation stress and reaches a much higher stress value than the experimental data does before beginning to transform to Martensite. After initial nucleation, the stress drops to a more stable level of approximately 700 MPa (around 4% total strain). The forward transformation stress also contains a significant amount of noise in the kMC–FEA model prediction.

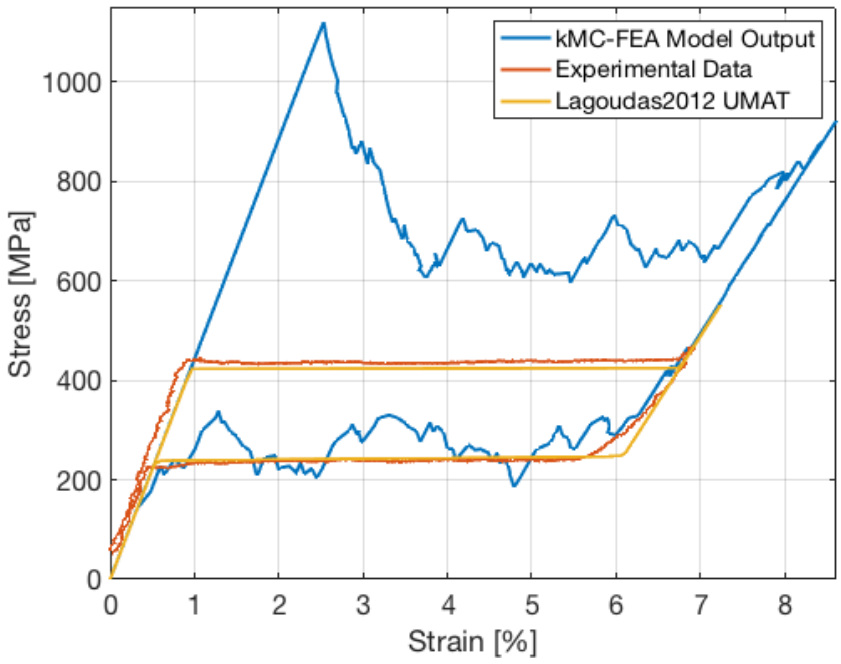

Figure 3.4: Comparison of the output from the uncalibrated kMC–FEA simulation output with experimental data and the calibrated Lagoudas 2012 SMA model

The experimental data and each model reach full transformation and load elastically in the Martensite phase, with both models fitting the experimental elastic loading data nearly exactly.

Upon unloading, the sample begins to transform back to Austenite. Like at the forward nucleation stress, the Lagoudas model predicts an abrupt change from elastic unloading to transformation at constant stress. The kMC–FEA model actually appears to more closely match the qualitative behavior of the experimental sample during this transition, because the transition from elastic unloading to phase transformation is more gradual in both the experimental data and in the kMC–FEA model prediction.

After this brief transition region, the Lagoudas model again fits the experimental data very closely in an almost constant-stress reverse transformation. The kMC–FEA model predicts an average stress at nearly the same value, but again with a significant amount of noise. Reverse transformation continues until the sample and each model have completely transformed back to their initial Austenite phase, recovering 100% of their transformation strain. The load cycle is completed when the experiment and each model unload elastically (and nearly identically), back to their original unstrained state.

The hysteresis stress predicted by the kMC–FEA method is about twice the magnitude as that shown in experiment and predicted by the Lagoudas model.

Overall, the Lagoudas model fits the experimental data very well, with slight deviations at the critical stresses. The kMC–FEA model does a fair job of matching the general behavior of the material and the character of the transition points. It does predict a very high forward stress value, and has a lot of noise. Discussion of the noisy transformation process is given in section 4.2.1. The kMC–FEA model output also appears to be quite different from experiment and the Lagoudas model during forward transformation. Note the large spike in elastic strain prior to transformation. Further discussion about the stress overshoot is given in section 4.2.2.

In its current state, a systematic optimization technique it not employed to fit the kMC–FEA model to experimental data due to project time and computational constraints. The results of such a data fitting scheme would undoubtedly be illustrative. However, to explore each new set of model parameters, a complete kMC–FEA simulation needs to be performed. This can take minutes, hours, or days to run on a personal workstation, depending on the size of the model and the parameter values. Future work, focusing on further validation of this model, should probably include such a numerical fitting operation, with a discussion of how/where it drives the relevant thermodynamic parameters and what the significance of that would be. Altering the software to run in parallel on a high-performance computing platform could significantly reduce the simulation time, making a parameter fitting routine more feasible.

A few additional simulations were performed, attempting to bring the outputs of the kMC–FEA model into closer agreement with experimental data. Some important observations can be made about the results. Increasing the mesh refinement reduces the stress noise during forward and reverse transformation. Significant hardening can be seen at the end of forward and reverse transformation on larger models with more refined meshes. This may be a mixed effect representing model sensitivity to the attempt frequency and the total number of transformation zones, but further investigation would be required to isolate these effects. Additionally, simulations containing a larger number of elements and transformation zones require more time to complete.

CHAPTER 4. DISCUSSION

4.1 kMC–FEA Model Behavior

As indicated in Figs. 5-7, the kMC-FEA model captures the basic behaviors of SMAs. Interestingly, the hysteretic features of the model are emergent from the simple model that the material transforms in small regions according to transition state theory, and knowledge of the energetics of the process. Here we discuss these emergent properties of the kMC–FEA model and their significance, followed by a discussion regarding individual model parameters and their effect on model outputs.

4.1.1 Emergent Hysteresis

The most notable result of this study is the emergence of superelastic stress and temperature hysteresis, as well as the shape memory effect at lower temperatures. The superelastic stress and temperature hysteresis are not surprising, given Chen's earlier work illustrating these behaviors [1, 2]. To our knowledge, the shape memory effect has not been previously demonstrated using kMC methods, but naturally follows from this model when the temperature operates below T_{AF}.

In a stress hysteresis loop, like that shown in Figure 3.1, the stress of forward transformation from Austenite to Martensite exceeds the stress of reverse transformation back from Martensite to Austenite. This is characteristic of superelastic shape memory alloys, and any SMA model should exhibit this property. The kMC–FEA model framework does not, however, enforce this hysteretic behavior. Rather, the stress hysteresis emerges when reasonable values for the transformation energy/entropy are used as parameter inputs. Hence, rather than prescribing superelastic stress hysteresis, the kMC–FEA model predicts superelasticity as the natural outcome of such conditions. Similarly, temperature hysteresis, like that shown in Figure 3.2, is also predicted as an emergent behavior of the kMC–FEA model.

The shape memory effect, as illustrated in Figure 3.3, is predicted by the kMC–FEA model under similar conditions to those used to produce superelastic hysteresis. Shape memory behavior is achieved by simply lowering the temperature of the simulation below the Austenite Finish temperature. Residual strain, generate through stress-induced transformation, is maintained through a lack of complete reverse transformation, but then completely recovered through thermally induced transformation. Simple demonstration of the shape memory effect with changing temperature is a good indication of the qualitative validity of such a model at predicting the physical nature of the material system.

4.1.2 Parameter Sensitivity

A major focus of this work has been to implement and explore a relatively new type of stochastic material model. For the kMC–FEA model to be useful, an understanding of the parameters and how they affect the model output is very important. Showing that the model responds predictably according to theory in at least one part of the parameter space was the primary accomplishment of the parameter study documented in section 3.2. The following section is a discussion of the individual model parameters and their influence on model behavior, as observed in the Parameter study and other simulations.

The transformation strain (ε^{tr} or γ_0 in single shear variant models) is the strain induced by transformation from Austenite to a variant of Martensite. This parameter governs the total extent to which the model can stretch due to transformation. It also plays a large role in determining the transformation energy and transformation rate, since the elastic inclusion energy (E_I) is a large portion of the total transformation energy and is a strong function of the transformation strain ($E_I \propto \gamma_0^2$).

The stiffness and Poisson's ratio (E_y & ν) of the material have the usual mechanical effects seen in the elastic portions of the stress-strain response. They also affect the transformation kinetics because they contribute directly to the elastic inclusion energy (E_I).

The transformation entropy (ΔS_0) plays a large role in determining the character of the transformation in that it determines the degree to which changes in temperature affect the transformation energy. Increasing the magnitude of ΔS_0 tends to shift the stress-strain hysteresis loop to higher stresses. Increasing the magnitude of ΔS_0 also tends to reduce the magnitude of the temper-

ature hysteresis and the degree to which the apparent equilibrium temperature shifts when stress is applied during thermal cycling.

The transformation volume (Ω_0) is of great physical significance and deserves more in-depth study than has been performed here. It is probably one parameter that could be determined experimentally by measuring the physical volume of the smallest regions that transform. For the purpose of this study, values of Ω_0 were selected after examining literature [42] and observing the behavior of kMC–FEA model simulations, though the selection is still somewhat arbitrary. With regards to model sensitivity to this parameter, it can be seen that increasing the transformation volume tends to reduce the stochastic effects of the model and make transformation occur more predictably. As shown in Equation 2.1, the transformation volume (along with the Boltzmann constant and the simulation temperature), determine to what extent different energy transformation events can occur. A very large transformation volume ensures that only the lowest energy transformation events occur, whereas a small transformation volume (or very high temperature) increase the relative probability of a wide range of higher energy events.

The transformation temperatures (T_A & T_M) obviously directly influence the temperatures at which the model transforms when under no applied stress loading. Increasing either parameter tends to decrease the apparent equilibrium stress for a given operating temperature and increasing the difference between the two ($T_A - T_M$) tends to increase the magnitude of the stress and temperature hysteresis.

The attempt frequency (ν_0) represents the maximum transformation rate for a given transformation zone. When the calculated activation energy of transformation drops to 0 or below, transformation zones transform at this rate. For this work, the attempt frequency was set to be approximately the Deybe frequency for the material. Experience working with this parameter showed that the model output is highly sensitive to this parameter in conjunction with the loading rate and the external time step parameter (Δt_{ext}).

These three parameters (ν_0, Δt_{ext}, and the loading rate) must be tuned well if good model behavior is desired. If the attempt frequency is set too high compared with the loading rate, the simulation comes to a pseudo-equilibrium in which the phases flips forward and backward at high rates and no hysteresis can occur (hysteresis is inherently a non-equilibrium process). However, if the attempt frequency is too low compared with the simulation loading rate, the loading essentially

outruns the phase transformation front, increasing the apparent transformation stress and making the model transform somewhat randomly, rather than through phase front propagation. Having a very high attempt frequency also tends to greatly increase the total time a simulation takes to run. This is due to the fact that increasing the attempt frequency generally increases the probability that any event will occur and shortens the internal time step (Δ_{int}). This, in turn, increases the total number of time steps and FEA calls required to complete the simulation. This problem is greatly accentuated when the loading rate is low and the model spends many kMC steps transforming back and forth between metastable configurations at a high rate. Chen refers to this as "phase flipping" [1] and suggests a remedy for reducing its effect which is not implemented in this model.

The maximum external time step (Δt_{ext}) governs the maximum amount of time that can occur between simulation time step. This is the time step which is prescribed by the kinetic Monte Carlo algorithm if the total calculated transformation rate is too low to predict a transformation event within this length of time. This parameter also must be tuned carefully to produce good model results since setting the value too low will prevent transformation from occurring at all and setting it too high may cause the simulation to overshoot critical transformation events. Although (Δt_{ext}) is not a physical material parameter, it nonetheless can have a significant effect on the model behavior. Further investigation of this parameter, its relation to the physics of the model, and a systematic approach to selecting an appropriate value for simulation are warranted for future study.

The least well-understood parameter is the so-called frictional energy (E_{fr}). It mainly serves as a fitting parameter at this point, since it is used to account for the unknown energy contributions to the barrier between phase states. It also serves to account for other energies which are not otherwise accounted for in this model – specifically the surface and interfacial energies – which it does poorly, since it is given as a constant in the model and does not include information about neighboring transformation regions, local free surfaces, etc. If other energies were accounted for separately, it might be possible to estimate E_{fr} by investigating the nature of the transformation at the atomic scale using density functional theory (such as in the work of [43]) or other means of investigating the transition state, but such investigation would require considerable effort.

4.2 Comparison with Experiment

Although not a perfect fit, the kMC–FEA model does capture some significant features of experimentally observed transformation. For instance, the average reverse transformation stress predicted by the kMC–FEA method is very comparable to the experimentally observed value. Additionally, it can be observed that the initiation of reverse transformation is more gradual than that of the abrupt transformation nucleation observed at the beginning of forward transformation. The kMC–FEA model predictions appear consistent with this experimental trend, whereas the Lagoudas phenomenological model does not seem to capture this smooth transition.

The forward transformation predictions made by the kMC–FEA model leave much to be desired in the way of experimental comparison, as they seem to be much too high. This may be an artifact of the finite element mesh, the initial conditions, or a lack of accounting for a crucial transformation energy neglected by the model. further discussion of the noisy nature of the transformation is given below in sections 4.2.1 and 4.2.2. Contrast this transformation with the behavior of the model simulations shown in Figures 3.1, 3.2, and 3.3 for superelastic hysteresis, thermal hysteresis, and the shape memory effect. The nature of these simulations is much smoother and more predictable. Obviously, the parameter inputs have a great deal of influence over the general nature of the model output which is not yet fully understood. It may be that high strain transformations, like those in the experimental comparison simulation, require a more accurate estimate the of inclusion energy (see discussion of E_I in section 4.4), since the inclusion energy becomes the dominant transformation energy contribution at this point.

4.2.1 Noisy Transformations

The predictions made by the kMC–FEA model for forward and reverse transformation processes observed during experimental comparison contained a lot of noise. This noise may be due to the small size of the finite element model used in simulation. The noise may also be attributed partially to the fact that the transformation strain (γ_0) for this comparison is much higher than the transformation strain used in other simulations, like those shown in Figures 3.1 – 3.3 (5.15% strain compared with 1.65% and 1.5%). This also dramatically increases the elastic inclusion energy (E_I)

and may be a significant factor in causing the behavior of the kMC–FEA model to be so erratic during transformation.

In an effort to reduce the amount of time required to obtain numerical output from simulations, and thus increase the number of experimental simulations performed during this study, the transformation volume used in the present study is a relatively large fraction of the total finite element volume. As such, a single transformation event has the ability to significantly impact the total stress–strain response of a simulation. This is especially apparent when large transformation strains, like those used in the simulation comparing the kMC–FEA model output with experimental data and the output of the fitted Lagoudas model are used. We hypothesize that performing comparable simulations with a larger, finer-meshed finite element model would greatly reduce the noise in the transformation stress. A limited number of simulations performed with more finely meshed finite element models seems to support this hypothesis.

4.2.2 Transformation Stress Overshoot

During forward transformation (from Austenite to Martensite), the kMC–FEA model tends to overshoot the transformation stress in a manner qualitatively similar to yield a point phenomenon during stress–strain loading. This is also sometimes observed, to a more limited degree, in experiments. A similar overshoot on the forward transformation of the transformation temperature is observed in the temperature–strain domain when thermal loading is applied during kMC–FEA simulation.

We postulate that this is due to the pristine nature of the finite element model (or experimental sample) before transformation nucleates. Due to the lack of inhomogeneity, surface energy, crystalline disorder, defects, etc. the strain energy required for homogeneous phase nucleation is higher than that required for phase front propagation. We believe this is not observed during reverse transformation because a disordered phase boundary already exists at the fringes of the FEA model where transformation is prohibited, providing heterogeneous nucleation sites. This is supported by the fact that reverse transformation initiates at these edges and that reverse transformation stresses more closely match experimental values.

Stresses predicted by this model may also be artificially high due to a lack of any other plasticity mechanism. Because only a single Martensite variant and no dislocation-based plasticity

mechanisms are functioning within this model framework, transformation stresses are not relieved via these mechanisms as they would be in experiment.

4.3 kMC–FEA Model Uses and Potential

The wide range of behaviors which the kMC–FEA model framework is capable of predicting highlight the power of of this relatively simple model. The kMC–FEA modeling approach is a more fundamental, "bottom up" approach to materials modeling and may help bridge the gap between first principles models, like Molecular Dynamics Simulation and Density Functional Theory, and higher-level phenomenological models or experimental observations.

With transformation energy and entropy values as inputs, this type of modeling technique has the ability to predict material behavior unknown *a priori* to the user. Similar to other, more basic first principles models, this kind of model may be used to perform numerical exploration of the parameter space, changing energy and entropy values, along with loading parameters, and observing novel outputs. Such numerical exploration may have the potential to lead to future, unforeseen discoveries in SMA science and engineering. Discovery and design of unique and desirable model outputs through combinations of model inputs may give helpful guidance to materials scientists and engineers for ways to improve state-of-the art SMA materials.

In its current state, the kMC–FEA model framework is not practical for use as a commercial method for design and engineering analysis, but should be used primarily in scientific investigations for the near future. One of the model's primary limitations is computational efficiency. What the model gains in predicting novel behavior, it pays for through the necessity of computing the full partition function and FEA solution at each kMC iteration. This makes the method relatively slow for any but the smallest of finite element meshes and the shortest of simulation times, compared with more time–efficient phenomenological methods like that of Lagoudas et al [7, 29, 32].

4.4 Model Improvements

This model could be improved through measuring/fixing of some of its key parameters. For instance, the fundamental transformation volume Ω_0 and the attempt frequency ν_0 play a key role in the kinetics of the model and thus affect the output of the model. Values for these

parameters were chosen somewhat arbitrarily for this study after surveying a range of values and picking values that produced favorable output. Further systematic numerical investigation of these parameters and their expected values would greatly benefit the future use of this model and similar models to come.

Significant improvement could be made in the estimation of the elastic inclusion energy (E_I), which may currently have significant error associated with free surface effects, non-uniform matrix stiffness effects, and effects due to the unequal stiffness of Austenite and Martensite phases. Although solutions to the Eshelby inclusion problem do exist for isolated inclusions transforming in a matrix of a different stiffness, due to the complex nature of these solutions and the fact that the simulation conditions would also not match these other idealized conditions, more simplified methods are used in this study.

Chen and Schuh [1, 2] chose to neglect this elastic inclusion energy in their model. In section 6.2 of [2] Chen proposes several methods for estimating the energy, but states that it is computationally limiting to obtain accurate enough predictions via these methods. More accurate and computationally efficient methods for estimating the increase in elastic potential energy due to transformation eigenstrain may exist, but are left for future study.

Further improvement could be made by implementing multiple available Martensite variants (or collections of variants) available for transformation. Although 3-Dimensional models and multiple Martensite variants were beyond the scope of the present work, future models which include more complex geometry and a more complete selection of Martensite variants could be highly informative.

CHAPTER 5. CONCLUSIONS

In this work, we implement a kinetic Monte Carlo – Finite Element Analysis method that models the material behavior of shape memory alloys in ScIFEN. The model, an extension of the model presented by Chen and Schuh [1,2], takes material properties and loading parameters as inputs and predicts the mechanical response of SMA materials to stress and/or thermal loading. We use the output of this model implementation to provide scientific insights, beyond those given by Chen and Schuh, into the behavior of SMA materials and the character of the kMC–FEA modeling framework in a number of ways:

- We provide an estimate for the elastic energy of transformation by applying the Eshelby inclusion problem to SMA transformation zones, show how the elastic energy is a significant portion of the total energy of SMA transformation, and derive theoretical expressions for how it relates to the behavioral output of the kMC–FEA model.

- We demonstrate the shape memory effect, predicted but not demonstrated by Chen and Schuh [1], alongside with the superelastic effect and thermal hysteresis, which emerge from the kMC–FEA model under the expected conditions for shape memory behavior to occur in SMAs. The relative ease with which these behaviors emerge from the model, given predictable changes in the loading patterns, speaks to the effectiveness of this modeling framework at describing the underlying mechanisms governing the alloy transformation.

- We verify the theoretically predicted behavior of the kMC–FEA model through a full-factorial numerical exploration of a limited region the parameter space. This study shows good agreement between theoretical predictions and numerical outputs. It also demonstrates that the model can be used to reasonably predict SMA behavior in previously unsampled regions of the parameter space. This predictive power may prove useful for future SMA research,

aimed at optimizing SMA composition for targeted use cases, such as embedded sensory particle research.

- We provide valuable insight into the model parameters, discussing each parameter and its contribution to the overall model behavior. This discussion may be invaluable for future work in tailoring SMA material composition for desired mechanical behavior. For instance, exploration of the frictional energy parameter E_{fr} reveals that increasing the the energy barrier to transformation has a strong propensity to increase the stress hysteresis and thermal hysteresis during loading. If a larger hysteresis is desired for SMA component functionality, methods should be sought to increase this barrier to transformation. This could potentially include doping the chemical composition of the alloy with a trace concentration of some soluble element to partially inhibit transformation.

- We provide a qualitative comparison of the kMC–FEA model framework with experimental results and predictions made by the phenomenological Lagoudas model [32]. We demonstrate that, given energy terms and a small amount of model fitting, a kMC–FEA model can loosely reproduce experimentally observed SMA tensile behavior. Further exploration and model refinement would be required to enable the kMC–FEA model to make high-fidelity quantitative predictions about component-scale SMA responses. For instance, the kMC–FEA model is still highly sensitive to some parameters such as the maximum time step (Δt_{ext}), the kMC attempt frequency (ν_0), and FEA mesh properties.

5.1 Statement of Personal Contribution

I made the following contributions to this project:

- Using the Eshelby inclusion equations, I derived the expression for the 2-Dimensional elastic energy of transformation given in equation 2.11. I found this helpful since it provided a concise way to include the elastic energy in the transformation rate calculation analytically in a way that revealed the contributions of the material stiffness, Poisson ratio, and transformation strain to the total elastic energy.

- To verify that the elastic energy calculation I derived matched the elastic energy predicted by the finite element software, I designed and executed the convergence study depicted in Figure 2.3. This also helped me make future judgment about sufficient mesh refinement for future simulations.

- While trying to predict and interpret the output of this new modeling scheme, I decided that it would be helpful to have a good approximation for the critical transformation stresses and temperatures. This would allow me to design more effective simulations, explore model behaviors, and would serve as a first step toward fitting simulation behavior to experimentally observed phenomena. To this end, I used the model kinetics and thermodynamic principles as a basis to derive equations (2.13 – 2.18) which predict transformation stresses and temperatures.

- To verify that the predictive equations I derived actually represented the behavior of the model in simulation, I designed and executed the parameter study documented in section 3.2. Although the project had other pressing issues, I felt this verification was an important part of the model development.

- Further exploration by comparison with experiments and the Lagoudas model predictions required that appropriate kMC–FEA model parameters be selected such that the simulation output would match the expected behavior. I devised the method of output fitting documented in section 2.3, which gives a systematic way to translate the Lagoudas model parameters into compatible kMC–FEA parameters

- Software implementation: I performed a significant portion of the necessary C++ and Python source code development for implementing the kMC–FEA model in ScIFEN. This included:

  - I used the existing orthotropic elastic material model class provided with the ScIFEN software package as a pattern to implement a new orthotropic elastic material model class with the capability of changing its stiffness and eigenstrain based on variable phase configuration and crystallographic orientation.
  - I used existing methods as a pattern to implement new methods for passing unique SMA material parameters from input scripts to the kMC–FEA solver. I Also used

existing output methods as a pattern to implement methods for exporting new model outputs to readable output files.

  - Because the Eshelby inclusion problem requires transformation zones to be ellipical (or ellipsoidal), I devised and implemented a routine which dynamically creates and tracks a super-mesh of transformation zones within the finite element mesh, composed of approximately ellipical (or ellipsoidal) groups of existing model integration points. This provided a highly versatile and robust meshing procedure that precluded the need to create a new finite element type specifically for this model. It also allows the user to run kMC–FEA procedures on existing meshes.

Notable contributions made by others:

- The kMC–FEA model framework for SMA materials was developed by Chen and Schuh
- Eric Homer provided much expertise and advice regarding the implementation of kMC–FEA methods. His guidance and feedback was essential throughout the research process
- Vesselin Yamakov provided insights into the relevant thermodynamics of the problem
- Collaborators at the NASA Langley Research Center developed the ScIFEN implicit finite element solver. They made the source code available and also responded quickly and helpfully to questions about altering the code.
- James Warner implemented variable time step FEA computation in ScIFEN
- Geoffrey Bomarito developed the Skeleton of the kMC algorithm in ScIFEN, allowing for eigenstrain enforcement and transformation bookkeeping
- Jake Hochhalter implemented a lot of the input/output routines which make simulation and data visualization possible. Jake also helped secure funding for the research
- Darren Hartl provided the experimental data and Lagoudas 2012 model prediction data.

REFERENCES

[1] Chen, Y., and Schuh, C. A., 2015. "A coupled kinetic Monte Carlo-finite element mesoscale model for thermoelastic martensitic phase transformations in shape memory alloys." *Acta Materialia,* **83**, pp. 431–447. ii, 1, 5, 6, 23, 29, 32, 36, 37

[2] Chen, Y., 2018. "Kinetic Monte Carlo Modeling of Martensitic Phase Transformation Dynamics." In *Handbook of Materials Modeling*. Springer International Publishing, Cham. ii, 1, 5, 6, 23, 29, 36, 37

[3] Cisse, C., Zaki, W., and Ben Zineb, T., 2016. "A review of constitutive models and modeling techniques for shape memory alloys." *International Journal of Plasticity,* **76**, jan, pp. 244–284. 1, 4

[4] Barbarino, S., Saavedra Flores, E. L., Ajaj, R. M., Dayyani, I., and Friswell, M. I., 2014. "A review on shape memory alloys with applications to morphing aircraft." *Smart Materials and Structures,* **23**(6), p. 063001. 2, 3

[5] Wagner, M. F. X., and Windl, W., 2008. "Lattice stability, elastic constants and macroscopic moduli of NiTi martensites from first principles." *Acta Materialia,* **56**(20), pp. 6232–6245. 2, 3

[6] Bhattacharya, K., 2003. *Microstructure of martensite. Why it forms and how give rise to the shape-memory effect.*. Oxford University Press. 3, 14

[7] Lagoudas, D. C., ed., 2008. *Shape Memory Alloys*., 1 ed., Vol. 1 Springer Science+Business Media, LLC, New York, NY. 3, 4, 35

[8] Mabe, J. H., Calkins, F. T., and Alkislar, M. B., 2008. "Variable area jet nozzle using shape memory alloy actuators in an antagonistic design." *Proceedings of SPIE - The International Society for Optical Engineering,* **6930**(June), pp. 69300T–69300T–12. 3

[9] Song, G., Ma, N., Lee, H. J., and Arnold, S., 2007. "Design and control of a proof-of-concept variable area exhaust nozzle using shape-memory alloy actuators." *Smart Materials and Structures,* **16**(4), aug, pp. 1342–1347. 3

[10] Hartl, D. J., and Lagoudas, D. C., 2007. "Aerospace applications of shape memory alloys." *Proceedings of the Institution of Mechanical Engineers, Part G: Journal of Aerospace Engineering,* **221**(4), pp. 535–552. 3

[11] Tian, W., Chen, Q., Liu, L., Chang, W., Zuo, X., Yang, H., Li, A., and Wang, L., 2006. "NiTi wire as a superelastic damping material in structural engineering." *Materials Science and Engineering: A,* **438-440**, nov, pp. 1089–1092. 3

[12] Hernandez, E. A. P., and Lagoudas, D. C., 2015. "Modeling size effects on the transformation behavior of shape memory alloy micropillars." *Journal of Micromechanics and Microengineering,* **25**(7), jul, p. 17. 3, 4

[13] Fernandes, D. J., Elias, C. N., Vidal, R., and Mendes, A. d. M., 2015. "Mechanical Performance of Nickel-titanium Archwires." *Materials Research,* **18**(6), nov, pp. 1264–1277. 3

[14] Nematzadeh, F., and Sadrnezhaad, S. K., 2013. "Effects of crimping on mechanical performance of nitinol stent designed for femoral artery: Finite element analysis." *Journal of Materials Engineering and Performance,* **22**(11), dec, pp. 3228–3236. 3

[15] Hochhalter, J. D., Leser, W. P., Newman, J. A., Glaessgen, E. H., Cornell, S. R., Willard, S. A., and Heber, G., 2014. Coupling Damage-Sensing Particles to the Digitial Twin Concept Tech. Rep. April, NASA STI, Hanover, MD 21076-1320. 3

[16] Hochhalter, J. D., Leser, W. P., Cornell, S. R., Newman, J. A., and Hartl, D. J., 2014. "Development and Characterization of Embedded Sensory Particles Using Multi-Scale 3D Digital Image Correlation." In *ASME 2014 International Design Engineering Technical Conferences & Smart Materials, Adaptive Structures and Intelligent Systems*, pp. 1–6. 3

[17] Leser, W. P., Newman, J. A., Hochhalter, J. D., Gupta, V. K., and Yuan, F. G., 2016. "Embedded Ni-Ti particles for the detection of fatigue crack growth in AA7050." *Fatigue and Fracture of Engineering Materials and Structures,* **39**(6), jun, pp. 686–695. 3, 4

[18] Yamakov, V., Hochhalter, J. D., Leser, W. P., Warner, J. E., Newman, J. A., Purja Pun, G. P., and Mishin, Y., 2016. "Multiscale modeling of sensory properties of CoNiAl shape memory particles embedded in an Al metal matrix." *Journal of Materials Science,* **51**(3), pp. 1204–1216. 3

[19] Cornell, S. R., Leser, W. P., Hochhalter, J. D., Newman, J. A., and Hartl, D. J., 2014. "Development and Characterization of Embedded Sensory Particles Using Multi-Scale 3D Digital Image Correlation." In *ASME 2014 International Design Engineering Technical Conferences & Smart Materials, Adaptive Structures and Intelligent Systems*. 3

[20] Bielefeldt, B. R., 2016. "Computational Analysis Of Shape Memory Alloy Sensory Particles For Structural Health Monitoring Applications." Master's thesis, Texas A&M. 3

[21] Bielefeldt, B. R., Benzerga, A. A., and Hartl, D. J., 2016. "Analysis of shape memory alloy sensory particles for damage detection via substructure and continuum damage modeling." In *Behavior and Mechanics of Multifunctional Materials and Composites 2016*, N. C. Goulbourne, ed., Vol. 9800, International Society for Optics and Photonics, p. 98000B. 3

[22] Bielefeldt, B., Hochhalter, J., and Hartl, D., 2016. "Computationally Efficient Analysis of SMA Sensory Particles Embedded in Complex Aerostructures Using a Substructure Approach." In *Proceedings of the ASME 2015 Conference on Smart Materials, Adaptive Structures and Intelligent Systems SMASIS2015*, pp. 1–10. 3

[23] Bielefeldt, B. R., Hochhalter, J. D., and Hartl, D. J., 2018. "Shape memory alloy sensory particles for damage detection: Experiments, analysis, and design studies." *Structural Health Monitoring,* **17**(4), jul, pp. 777–814. 3

[24] Chowdhury, P., and Sehitoglu, H., 2017. "Deformation physics of shape memory alloys Fundamentals at atomistic frontier." *Progress in Materials Science,* **88**, jul, pp. 49–88. 3

[25] Ko, W.-S., Grabowski, B., and Neugebauer, J., 2015. "Development and application of a Ni-Ti interatomic potential with high predictive accuracy of the martensitic phase transition." *Physical Review B,* **92**(13), p. 134107. 3

[26] Ko, W.-S., Maisel, S. B., Grabowski, B., Jeon, J. B., and Neugebauer, J., 2017. "Atomic scale processes of phase transformations in nanocrystalline NiTi shape-memory alloys." *Acta Materialia,* **123**, pp. 90–101. 3

[27] Mirzaeifar, R., Gall, K., Zhu, T., Yavari, A., and Desroches, R., 2014. "Structural transformations in NiTi shape memory alloy nanowires." *Journal of Applied Physics,* **115**(19), may, p. 194307. 3

[28] Zhong, Y., Gall, K., and Zhu, T., 2012. "Atomistic characterization of pseudoelasticity and shape memory in NiTi nanopillars." *Acta Materialia,* **60**(18), pp. 6301–6311. 3

[29] Lagoudas, D. C., Bo, Z., and Qidwai, M. A., 1996. "A unified thermodynamic constitutive model for SMA and finite element analysis of active metal matrix composites." *Mechanics of Composite Materials and Structures,* **3**(2), pp. 153–179. 4, 16, 35

[30] Boyd, J. G., and Lagoudas, D. C., 1996. "A thermodynamical constitutive model for shape memory materials. Part II. The SMA composite material." *International Journal of Plasticity,* **12**(7), pp. 843–873. 4

[31] Boyd, J. G., and Lagoudas, D. C., 1996. "A thermodynamical constitutive model for shape memory materials. Part I. The monolithic shape memory alloy." *International Journal of Plasticity,* **12**(6), pp. 805–842. 4

[32] Lagoudas, D., Hartl, D., Chemisky, Y., MacHado, L., and Popov, P., 2012. "Constitutive model for the numerical analysis of phase transformation in polycrystalline shape memory alloys." *International Journal of Plasticity,* **32-33**, pp. 155–183. 4, 16, 35, 38

[33] Scholten, W. D., Patterson, R. D., Hartl, D. J., Strganac, T. W., Chapelon, Q. H. C., and Turner, T., 2017. "Computational and Experimental Fluid-Structure Interaction Analysis of a High-Lift Wing with a Slat-Cove Filler for Noise." In *2017 AIAA SciTech Forum*, American Institute of Aeronautics and Astronautics, p. 13. 4, 16

[34] Scholten, W., Turner, T., Eustice, M., Patterson, R., Cook, S., Hartl, D., and Strganac, T., 2018. "Aerodynamic and Structural Evaluation of an SMA Slat-Cove Filler Using Computational and Experimental Tools at Model Scale." In *Conference on Smart Materials, Adaptive Structures and Intelligent Systems SMASIS2018*, ASME 2018, p. V001T04A019. 4

[35] Arena, G., Groh, R., Pirrera, A., Scholten, W., Hartl, D., and Turner, T., 2018. "A Tailored Nonlinear Slat-Cove Filler for Airframe Noise Reduction." In *Conference on Smart Materials, Adaptive Structures and Intelligent Systems SMASIS2018*, ASME 2018, p. 13. 4

[36] Bulatov, V. V., and Argon, A. S., 1994. "A stochastic model for continuum elasto-plastic behavior: I. numerical approach and strain localization." *Modelling and Simulation in Materials Science and Engineering,* **2**(2), mar, pp. 167–184. 6

[37] Homer, E. R., and Schuh, C. A., 2009. "Mesoscale modeling of amorphous metals by shear transformation zone dynamics." *Acta Materialia,* **57**(9), pp. 2823–2833. 6, 12

[38] Eshelby, J. D., 1957. "The Determination of the Elastic Field of an Ellipsoidal Inclusion, and Related Problems." *Proceedings of the Royal Society A: Mathematical, Physical and Engineering Sciences,* **241**(1226), aug, pp. 376–396. 9

[39] Lubarda, V. A., and Markenscoff, X., 1998. "On the absence of Eshelby property for non-ellipsoidal inclusions." *International Journal of Solids and Structures,* **35**(25), sep, pp. 3405–3411. 11

[40] Warner, J. E., Bomarito, G. F., and Hochhalter, J. D., 2016. Scalable Implementation of Finite Elements by NASA _ Implicit (ScIFEi), NASA/TM - 2016-219180 Tech. Rep. April, NASA Langley Research Center, Hampton, VA. 15

[41] ASTM International, 2016. ASTM E345-16 Standard Test Methods of Tension Testing of Metallic Foil Tech. rep., ASTM International, West Conshohocken, PA. 16

[42] Waitz, T., Kazykhanov, V., and Karnthaler, H. P., 2004. "Martensitic phase transformations in nanocrystalline NiTi studied by TEM." *Acta Materialia,* **52**(1), pp. 137–147. 31

[43] Zarkevich, N. A., and Johnson, D. D., 2014. "Shape-memory transformations of NiTi: Minimum-energy pathways between austenite, martensites, and kinetically limited intermediate states." *Physical Review Letters,* **113**(26). 32

APPENDIX A. PARTIAL DERIVATIVES OF CRITICAL STRESSES

$$\frac{\partial \tau_{MS}}{\partial T} = \frac{-\Delta S_0}{\gamma_0} \tag{A.1}$$

$$\frac{\partial \tau_{MS}}{\partial \Delta S_0} = \frac{-(T - T_0)}{\gamma_0} \tag{A.2}$$

$$\frac{\partial \tau_{MS}}{\partial E_{fr}} = \frac{2}{\gamma_0} \tag{A.3}$$

$$\frac{\partial \tau_{MS}}{\partial \gamma_0} = \frac{1}{\gamma_0^2}\Big(\Delta S_0(T - T_0) - 2E_{Fr} - E_I\Big) + \frac{1}{\gamma_)}\frac{\partial E_I}{\partial \gamma_0} \tag{A.4}$$

$$\frac{\partial \tau_{AS}}{\partial T} = \frac{\Delta S_0}{\gamma_0} \tag{A.5}$$

$$\frac{\partial \tau_{AS}}{\partial \Delta S_0} = \frac{T - T_0}{\gamma_0} \tag{A.6}$$

$$\frac{\partial \tau_{AS}}{\partial E_{fr}} = \frac{-2}{\gamma_0} \tag{A.7}$$

$$\frac{\partial \tau_{AS}}{\partial \gamma_0} = \frac{1}{\gamma_0^2}\Big(\Delta S_0(T - T_0) + 2E_{Fr} + E_I\Big) - \frac{1}{\gamma_)}\frac{\partial E_I}{\partial \gamma_0} \tag{A.8}$$

$$\frac{\partial \Delta \tau_H}{\partial T} = 0 \tag{A.9}$$

$$\frac{\partial \Delta \tau_H}{\partial \Delta S_0} = 0 \tag{A.10}$$

$$\frac{\partial \Delta\tau_H}{\partial E_{fr}} = \frac{4}{\gamma_0} \tag{A.11}$$

$$\frac{\partial \Delta\tau_H}{\partial \gamma_0} = \frac{-2}{\gamma_0^2}(E_I + 2E_{fr}) + \frac{2}{\gamma_0}\frac{\partial E_I}{\partial \gamma_0} \tag{A.12}$$

APPENDIX B. EXAMPLE KMC–FEA SCIFEN INPUT SCRIPT

```
#!/usr/bin/python
import h5py
from scifenpy.sierrahdf5 import Sierra as SH5

model_length = 60.0
eps1 = -0.01
eps2 = 0.06
KMC_T = 500.0 #[K]
T1 = KMC_T
T2 = KMC_T

max_dt = 0.01 #[ps]
num_steps = 100

tf = 1.0

KMC_a = 2.5           # [m] Transformation Zone radius
KMC_nu_0 = 1.0831e2   # [THz] Attempt frequency
KMC_Omega_0 = 1e-25   # [m^3] Transformation Volume
KMC_A = 280.0         # [K] Austenite Temperature
KMC_M = 240.0         # [K] Martensite Temperature
KMC_k = k = 1.381e-29 # [MPa*m^3/K] Boltzmann's Constant
KMC_H = 0.0515        # Maximum transformation strain magnitude
KMC_Delta_S = -0.35   # [MPa/K] Stress Influence Coefficient
KMC_E_fr = 4.2        # [MPa] Frictional Energy Barrier
KMC_E_fr_inter = 0    # [MPa] Inter-variant Energy Barrier
```

```
KMC_EA = 44200
KMC_EM = 26400
KMC_Ey = 0.5*(KMC_EA + KMC_EM)
KMC_nu = 0.33
KMC_E_I = 0.25*KMC_Ey * KMC_H * KMC_H / (1 - KMC_nu*KMC_nu)

with open('Results.txt', 'a+') as f:
    f.write('Temperature\t%e\n'% KMC_T +\
            'Delta_S_0\t%e\n' % KMC_Delta_S +\
            'E_friction\t%e\n' % KMC_E_fr +\
            'Omega_0\t\t%e\n' % KMC_Omega_0 +\
            'KMC_a\t\t%e\n'  % KMC_a +\
            'nu_0\t\t%e\n'   % KMC_nu_0 +\
            'KMC_k\t\t%e\n'  % KMC_k +\
            'KMC_H\t\t%e\n'  % KMC_H +\
            'max_dt\t\t%e\n' % max_dt +\
            'Load_Rate\t%e\n' % ((sigma2-sigma1)/(0.5*tf)) +\
            'E_I\t\t%e\n'    % KMC_E_I )

with h5py.File('input.h5', 'w', libver='latest') as h5:

    SH5.title(h5.id, '2D_dogbone Model')

    # materials
    E_A = KMC_EA #[MPa]
    E_M = KMC_EM #[MPa]
    nu = KMC_nu
    G_A = E_A/(2*(1+nu))
    G_M = E_M/(2*(1+nu))

    m = SH5.property_specification_for_material(h5.id, 'KMC_Mat', 2e-4)
```

```
SH5.parameters_for_model_sma(m, E_A, E_A, E_A,
                             nu, nu, nu,
                             G_A, G_A, G_A,
                             E_M, E_M, E_M,
                             nu, nu, nu,
                             G_M, G_M, G_M,
                             phi1=0, Phi=0, phi2=0,
                             phase=0)

# sections
s = SH5.solid_section(h5.id, 'section1', 'DEFAULT', 'FULL')

# finite element models

m = SH5.finite_element_model(h5.id, '2D_dogbone', 'scifen.h5m', 'MOAB')
p = SH5.parameters_for_block(m, 'ElementBlock1',
                             ['e_ALL_ELEM', ],
                             'KMC_Mat',
                             'section1')
SH5.active_for_procedure(p, 'PROC1', ['time_block_1'])

# output scheduler
o = SH5.output_scheduler(h5.id, 'schedule1', 0, tf)
SH5.at_step_increment(o, 0, 1)

# procedure
proc = SH5.scifei_procedure(h5.id, 'PROC1')
tc = SH5.time_control(proc, tf)
tsb = SH5.time_stepping_block(tc, 'time_block_1', 0.0)
SH5.parameters_for_scifei_region(tsb, 'region1', time_increment=tf/num_steps)

# region
```

```
reg = SH5.scifei_region(proc, 'region1', '2D_dogbone')

# Boundary Conditions
fdy = SH5.fixed_displacement(reg, components=('XYZ'))
SH5.node_set(fdy, ['n_XMIN_GRIPS'])
SH5.active_periods(fdy, ['time_block_1'])

fdy = SH5.fixed_displacement(reg, components=('YZ'))
SH5.node_set(fdy, ['n_XMAX_GRIPS'])
SH5.active_periods(fdy, ['time_block_1'])

fdy = SH5.fixed_displacement(reg, components=('Z'))
SH5.node_set(fdy, ['n_ZMIN'])
SH5.active_periods(fdy, ['time_block_1'])

# functions
SH5.definition_for_function(h5.id, 'KMC_ACTIVE', 'PIECEWISE LINEAR',
    [(0,1),(1*tf,1)])
SH5.definition_for_function(h5.id, 'KMC_a', 'PIECEWISE LINEAR',
    [(0,KMC_a),(1,KMC_a)])
SH5.definition_for_function(h5.id, 'KMC_nu_0', 'PIECEWISE LINEAR',
    [(0,KMC_nu_0),(1,KMC_nu_0)])
SH5.definition_for_function(h5.id, 'KMC_Omega_0', 'PIECEWISE LINEAR',
    [(0,KMC_Omega_0),(1,KMC_Omega_0)])
SH5.definition_for_function(h5.id, 'KMC_A', 'PIECEWISE LINEAR',
    [(0,KMC_A),(1,KMC_A)])
SH5.definition_for_function(h5.id, 'KMC_M', 'PIECEWISE LINEAR',
    [(0,KMC_M),(1,KMC_M)])
SH5.definition_for_function(h5.id, 'KMC_k', 'PIECEWISE LINEAR',
    [(0,KMC_k),(1,KMC_k)])
SH5.definition_for_function(h5.id, 'KMC_H', 'PIECEWISE LINEAR',
    [(0,KMC_H),(1,KMC_H)])
```

```
SH5.definition_for_function(h5.id, 'KMC_Delta_S', 'PIECEWISE LINEAR',
    [(0,KMC_Delta_S),(1,KMC_Delta_S)])
SH5.definition_for_function(h5.id, 'KMC_E_fr', 'PIECEWISE LINEAR',
    [(0,KMC_E_fr),(1,KMC_E_fr)])
SH5.definition_for_function(h5.id, 'KMC_E_fr_inter', 'PIECEWISE LINEAR',
    [(0,KMC_E_fr_inter),(1,KMC_E_fr_inter)])
SH5.definition_for_function(h5.id, 'KMC_E_I', 'PIECEWISE LINEAR',
    [(0,KMC_E_I),(1,KMC_E_I)])
SH5.definition_for_function(h5.id, 'KMC_E_A', 'PIECEWISE LINEAR',
    [(0,E_A),(1,E_A)])
SH5.definition_for_function(h5.id, 'KMC_E_M', 'PIECEWISE LINEAR',
    [(0,E_M),(1,E_M)])
SH5.definition_for_function(h5.id, 'KMC_nu', 'PIECEWISE LINEAR',
    [(0,nu),(1,nu)])
SH5.definition_for_function(h5.id, 'MAX_dt', 'PIECEWISE LINEAR',
    [(0,max_dt),(1,max_dt)])
SH5.definition_for_function(h5.id, 'TEMPERATURE', 'PIECEWISE LINEAR',
    [(0*tf,T1), (0.75*tf,T1), (1.0*tf,T2)])
SH5.definition_for_function(h5.id, 'stress_cycle', 'PIECEWISE LINEAR',[(0*tf,
    0.0), (0.00001*tf, sigma1), (0.5*tf, sigma2), (1*tf, sigma1)])
SH5.definition_for_function(h5.id, 'strain_cycle', 'PIECEWISE LINEAR',
    [(0*tf,0.0), (0.001*tf,eps1), (0.5*tf,eps2), (1*tf, eps1)])

SH5.define_direction(h5.id, 'unit_x', [1, 0, 0])

# Apply Prescribed displacement
pd = SH5.prescribed_displacement(reg, 'strain_cycle', component='X',
    scale_factor=model_length)
SH5.node_set(pd, ['n_XMAX_GRIPS', ])
SH5.active_periods(pd, ['time_block_1'])

# Solver
```

```
    sln = SH5.solver(reg,'PETSC')
    SH5.set_petsc_option(sln, 'ksp_type', 'preonly')
    SH5.set_petsc_option(sln, 'pc_type', 'lu')
    SH5.set_petsc_option(sln, 'pc_factor_mat_solver_package', 'mumps')

    ro = SH5.results_output(reg, '2D_dogbone OUTPUT', '2D_dogbone.out.h5m',
                            title='2D_dogbone', #steps_per_file=1,
                            exposed_surface=True, scheduler_name='schedule1')
    SH5.node_variables(ro, 'displacement', 'u')
    SH5.node_variables(ro, 'reaction', 'rf')
    SH5.node_variables(ro, 'phase', 'phase')
    SH5.node_variables(ro, 'rate', 'rate')

    SH5.element_variables(ro, 'phase', dbase_variable_name='phase')
    SH5.element_variables(ro, 'rate', dbase_variable_name='rate')
    SH5.element_variables(ro, 'stress', 'stress')
    SH5.element_variables(ro, 'strain', 'strain')

# Input file error checking
from scifenpy import Region
r = Region("input.h5")
ipass = r.check()
print ipass
```